



Numerical Hopkinson Bar Analysis: Uni-Axial Stress and Planar Bar-Specimen Interface Conditions by Design

by Bazle A. Gama and John W. Gillespie, Jr.

ARL-CR-553

September 2004

prepared by

**University of Delaware
Center for Composite Materials
Newark, DE 19716**

under contract

DAAD19-01-2-0005

NOTICES

Disclaimers

The findings in this report are not to be construed as an official Department of the Army position unless so designated by other authorized documents.

Citation of manufacturer's or trade names does not constitute an official endorsement or approval of the use thereof.

Destroy this report when it is no longer needed. Do not return it to the originator.

Army Research Laboratory

Aberdeen Proving Ground, MD 21005-5069

ARL-CR-553**September 2004**

Numerical Hopkinson Bar Analysis: Uni-Axial Stress and Planar Bar-Specimen Interface Conditions by Design

Bazle A. Gama and John W. Gillespie, Jr.
University of Delaware
Center for Composite Materials
Newark, DE 19716

prepared by

University of Delaware
Center for Composite Materials
Newark, DE 19716

under contract

DAAD19-01-2-0005

REPORT DOCUMENTATION PAGE			Form Approved OMB No. 0704-0188	
Public reporting burden for this collection of information is estimated to average 1 hour per response, including the time for reviewing instructions, searching existing data sources, gathering and maintaining the data needed, and completing and reviewing the collection information. Send comments regarding this burden estimate or any other aspect of this collection of information, including suggestions for reducing the burden, to Department of Defense, Washington Headquarters Services, Directorate for Information Operations and Reports (0704-0188), 1215 Jefferson Davis Highway, Suite 1204, Arlington, VA 22202-4302. Respondents should be aware that notwithstanding any other provision of law, no person shall be subject to any penalty for failing to comply with a collection of information if it does not display a currently valid OMB control number. PLEASE DO NOT RETURN YOUR FORM TO THE ABOVE ADDRESS.				
1. REPORT DATE (DD-MM-YYYY) September 2004		2. REPORT TYPE Final		3. DATES COVERED (From - To) January 2003–May 2003
4. TITLE AND SUBTITLE Numerical Hopkinson Bar Analysis: Uni-Axial Stress and Planar Bar-Specimen Interface Conditions by Design			5a. CONTRACT NUMBER DAAD19-01-2-0005	
			5b. GRANT NUMBER	
			5c. PROGRAM ELEMENT NUMBER	
6. AUTHOR(S) Bazle A. Gama* and John W. Gillespie, Jr.*			5d. PROJECT NUMBER 622618.AH80	
			5e. TASK NUMBER	
			5f. WORK UNIT NUMBER	
7. PERFORMING ORGANIZATION NAME(S) AND ADDRESS(ES) University of Delaware Center for Composite Materials Newark, DE 19716			8. PERFORMING ORGANIZATION REPORT NUMBER	
9. SPONSORING/MONITORING AGENCY NAME(S) AND ADDRESS(ES) U.S. Army Research Laboratory ATTN: AMSRL-WM-MB Aberdeen Proving Ground, MD 21005-5066			10. SPONSOR/MONITOR'S ACRONYM(S) ARL-CR-553	
			11. SPONSOR/MONITOR'S REPORT NUMBER(S)	
12. DISTRIBUTION/AVAILABILITY STATEMENT Approved for public release; distribution is unlimited.				
13. SUPPLEMENTARY NOTES *University of Delaware, Center for Composite Materials, Newark, DE 19716				
14. ABSTRACT High strain rate characterization of materials is usually performed using the Split Hopkinson Pressure Bar (SHPB) in the strain rate range, $10^2 - < 10^4$. In the one-dimensional analysis of Hopkinson bar experiment, it is assumed that the specimen deforms under uni-axial stress, the bar-specimen interfaces remain planar at all-time, and the stress equilibrium in the specimen is achieved in travel times. The first two assumptions are in general not true for acoustically hard specimens with diameter smaller than the bars. Explicit dynamic finite element analyses are used to investigate these assumptions. A new specimen design is suggested which satisfies the uni-axial stress condition in the specimen under the linear-elastic deformation phase of the specimen. A new Hopkinson bar experimental technique is presented to ensure that the bar-specimen interfaces remain planar at all time. Extensive numerical analyses are performed to quantify the accuracy of the proposed configurations.				
15. SUBJECT TERMS SHPB, numerical simulation, 3-D analysis, uni-axial stress, specimen design, planar bar-specimen interface, transmission tube				
16. SECURITY CLASSIFICATION OF:			17. LIMITATION OF ABSTRACT UL	18. NUMBER OF PAGES 58
a. REPORT UNCLASSIFIED	b. ABSTRACT UNCLASSIFIED	c. THIS PAGE UNCLASSIFIED		
			19b. TELEPHONE NUMBER (Include area code) 302-831-8352	

Contents

List of Figures	iv
List of Tables	v
Acknowledgments	vi
1. Introduction	1
1.1 SHPB Specimen Design	1
1.1.1 Specimen Design to Minimize Friction and Inertia	2
1.1.2 Experimental Study on Specimen Shape and Failure	4
1.2 Objectives	6
2. Numerical Simulation of Compression SHPB Experiment	6
3. Effect of Nonplanar Bar-Specimen Interface: The Problem	9
4. Uni-Axial Stress Along the Specimen Through Specimen Design: Partial Solution	10
4.1 Specimen Design 1: Cylindrical Specimen With Chamfered Edges.....	11
4.2 Specimen Design 2: Dog Bone/Dumbbell-Shaped Cylindrical Specimen.....	15
5. Planar Bar-Specimen Interface Condition Through Experiment Design: Complete Solution	19
5.1 Compression SHPB With a TT	19
5.2 Numerical Simulation of Compression SHPB With TT	22
6. Summary	30
7. References	31
Distribution List	35

List of Figures

Figure 1. Damage at the impact end of Takeda's unidirectional specimen at different loading levels.	4
Figure 2. Dog bone-shaped hollow cylindrical specimen geometry for torsional testing.	5
Figure 3. New compression SHPB specimen geometry proposed by Deltort et al. All dimensions in millimeters.	5
Figure 4. Schematic diagram of a compression SHPB and the notations used in the analyses.	7
Figure 5. Quartersymmetric model of SHPB and finite element mesh.	7
Figure 6. Loading history on the impact face of the IB.	9
Figure 7. Nonplanar bar-specimen interface deformation model of a small diameter hard specimen: u_i^j – axial displacements in Z-direction; subscripts $i = C, D$, and E represent bar-center, specimen-edge, and bar-edge, respectively; superscripts $j = 1$ and 2 ; “1” = IB-S interface; “2” = S-TB interface.	10
Figure 8. Numerical Hopkinson bar responses for two different test cases.	11
Figure 9. Contours of axial stress distribution in the specimen at a different time.	12
Figure 10. Quartersymmetric finite element model of Hopkinson bars and cylindrical ceramic specimen with chamfered edges, $D_s / D_b = 0.60$, $H_s / D_s = 1.00$, $\hat{D}_s = 0.60$	13
Figure 11. Axial stress distribution on the surface of ceramic specimen at a different time, $\hat{t} = t / T$, $\hat{D}_s = 0.60$, $r / R = 1.00$, $\sigma_{Z-IB}^{Max} = P_{max} = 500$ MPa.	13
Figure 12. Distribution of dimensionless axial stress along the length of a cylindrical specimen with and without chamfered edges.	14
Figure 13. Distribution of axial stress in the radial direction at different Z / H locations of a cylindrical specimen with chamfered edges, $\hat{t} = t / T = 0.25$	15
Figure 14. The parametric definition of a cylindrical dog bone/dumbbell-shaped specimen proposed by Deltort et al.	16
Figure 15. Contours of axial stress distribution in the dog bone-shaped specimen at a different time.	17
Figure 16. Distribution of dimensionless axial stress along the length of a dog bone-shaped specimen and that for cylindrical specimens with and without chamfered edges.	18
Figure 17. Deviation from stress equilibrium of different specimen designs.	18
Figure 18. A new compression SHPB experimental set-up with TT.	20
Figure 19. Finite element model of the compression SHPB with TT.	22
Figure 20. Bar responses of the new compression SHPB with TT.	24
Figure 21. Notations for axial displacements measured at different radial locations of different bars.	24
Figure 22. Nonplanar interface parameter, \hat{u}_i , as a function of time, ceramic specimen.	25

Figure 23. Nonplanar interface parameter, \hat{u}_i , as a function of time, aluminum specimen.....	25
Figure 24. HPB with TT: applications with direct impact and hollow cylindrical specimen.....	28
Figure 25. Deviation from the stress equilibrium of the ceramic specimen with a different H_S / D_S ratio, SHPB with TT.....	29
Figure 26. Stress-strain response of SHPB with TT and comparison with classic methods, H_S / D_S , $D_S / D_{IB} = 0.60$	30

List of Tables

Table 1. Geometric properties of the SHPB.	8
Table 2. Linear-elastic and elastic-plastic material constants.....	8
Table 3. Nonplanar bar-specimen interface parameters and fitting constants for ceramic specimen and steel bars.....	26
Table 4. Nonplanar bar-specimen interface parameters and fitting constants for the aluminum specimen and steel bars.	27

Acknowledgments

This report is prepared through participation in the Composite Materials Technology Collaborative Program sponsored by the U.S. Army Research Laboratory under Cooperative Agreement DAAD19-01-2-0005. The authors gratefully acknowledge the help provided by Dr. Libo Ren in data reduction, using the dispersion correction software “Hopkinson” developed by himself and coworkers at the University of Delaware-Center for Composite Materials. Discussion and difference in opinion with Dr. Sergey L. Lopatnikov generated new ideas of Hopkinson bar experiments and analysis, and is gratefully acknowledged.

1. Introduction

Hopkinson bar experimental techniques (1–5) are considered the simplest high strain rate test method compared to plate impact (4) and explosive loading techniques (4, 6). Significant advances have been made in the Hopkinson Bar research field to accommodate new test methods (7–9) and new analyses techniques (10, 11). A recent critical review by the authors elucidating the 20th century advancement in Hopkinson bar techniques (12) pointed out some further areas that need improvement prior to becoming a standard test method. Two such areas are considered in the present study: the specimen deforming under uni-axial stress and the bar-specimen interfaces remaining planar throughout the duration of the test.

Finite element analysis (FEA) has been performed to study the validity of one-dimensional (1-D) assumptions (13) of compression split-Hopkinson Pressure Bar (SHPB) technique. It has been identified that the nonplanar bar-specimen assumption made in Hopkinson Bar analysis is not valid for an acoustically hard specimen with diameter smaller than the bar. As a consequence, the average strain of the specimen measured from the bar response is found unreliable. The axial stress distribution of the specimen is found to be nonuniform in the linear elastic phase of deformation; however, it is uniform in the plastic phase. It has been identified that the stress equilibrium in an elastic-plastic specimen is not achieved in the linear elastic phase of deformation; however, the deviation from equilibrium in the plastic deformation phase is constant and minimum but not absolutely zero. These important observations focused our efforts on identifying mechanisms to achieve uni-axial stress via design of the specimen geometry while simultaneously minimizing the nonplanar deformation of the bar-specimen interfaces via modifications to the test fixturing. Our objective is to achieve more accurate strain measurements enabling high strain rate properties in the elastic regime to be measured reliably.

1.1 SHPB Specimen Design

Historically, right circular cylindrical specimens have been used in the compression testing of isotropic elastic-plastic materials. However, researchers have looked at many different specimen geometries while conducting tension, shear, and torsion testing of materials under Hopkinson bar loading (4). Top hat specimen geometry for measuring tension properties using the compression SHPB is described by Lindholm and Yeakley (14). Dog bone-shaped cylindrical (15, 16) and strip specimens (17–20) have been used in tension split SHPB testing. A double-notch-shear (DNS) testing (21) and punch loading (22) are described in reference (4), where an incident bar and a transmitter tube are used in conjunction with double-notch and flat-plate specimens. A hat-shaped specimen can also be used with traditional SHPB for shear testing (4). Dog bone-shaped tubular specimens, on the other hand, are generally used for torsion testing (23) at high loading rates.

1.1.1 Specimen Design to Minimize Friction and Inertia

Specimen design with the objectives of minimizing friction and inertia effects has also been looked at in the past by many researchers. The maximum specimen diameter (D_s) that can be allowed is equal to the bar diameter (D_B). Gray (24) suggested that the radial and longitudinal inertia and friction effects can be lessened by minimizing the areal-mismatch between the bar and specimen ($D_s \sim 0.80D_B$); and choosing H_s/D_s ratio (H_s – length of the specimen) between 0.50 and 1.0, which is based on the corrections for inertia effects proposed by Davies and Hunter (25):

$$\sigma_s^C(t) = \sigma_s^M(t) + \rho_s \left[\left(H_s^2/6 \right) - \left(v_s D_s^2/8 \right) \right] \times \left(\partial^2 \epsilon(t) / \partial t^2 \right), \quad (1)$$

where subscript S stands for “specimen,” and superscripts C and M stand for “corrected” and “measured,” respectively. This expression predicts that the correction term will be zero, if either the strain rate is constant or the bracketed term is zero. The later condition provides the optimum ratio of the specimen for inertia effect and is expressed as follows:

$$H_s/D_s = \sqrt{3v_s/4} \quad (2)$$

For a Poisson’s ratio of 0.333, the optimum H_s/D_s is 0.50. To minimize the friction effects, the H_s/D_s ratio should be in the range 1.50–2.00 (26). Thus the conditions for minimum friction and inertia effects cannot be satisfied simultaneously and Gray’s (24) suggestion of $0.50 < H_s/D_s < 1.0$ can be taken as a compromise between these two effects.

If a constant strain rate condition is used, then one can effectively use thinner specimens ($H_s/D_s < 0.50$), and thus minimize the stress nonequilibrium in the specimen. Usually, constant strain rate conditions can be achieved through shaped incident pulses; however, the attainable strain rates in these cases are limited by the stress rate of the incident pulse (27). The optimum thickness of the specimen depends on the rise time, t , required to achieve a uni-axial stress state in the specimen. The rise time is estimated as the time required for π reverberations in the specimen (26). For a plastically deforming solid that obeys the Taylor-von Karman Theory, the rise time is given by

$$t^2 \geq (\pi^2 \rho_s H_s^2) / (\partial \sigma / \partial \epsilon), \quad (3)$$

where ρ_s and H_s are the density and thickness of the specimen, respectively, and $\partial \sigma / \partial \epsilon$ is the stage 2 work-hardening rate of the true stress-strain diagram of the material to be tested. By decreasing the specimen thickness, it is thus possible to reduce the rise time; however, the specimen H_s/D_s requirement for minimizing friction and inertia effects requires that the specimen diameter also be reduced. Consequently, one needs to use a smaller diameter bar as well (to satisfy the conditions, $D_s \sim 0.80D_B$ and $0.50 < H_s/D_s < 1.0$).

Malinowski and Klepaczko (28) presented a combined analytical, experimental and numerical study in the determination of an optimum specimen geometry used in the SHPB test technique. In addition to specimen inertia investigated by Davies and Hunter (25), the effect of interfacial friction between the Hopkinson bars and a cylindrical specimen is considered in the analysis. A unified approach to inertia and friction is offered through the consideration of energy balance. The difference between the measured (σ_s^M) and correct (σ_s^C) specimen stress using “3-wave” analysis can be expressed as follows:

$$\sigma_s^M - \sigma_s^C = \frac{\mu \sigma_s^M}{3 \cdot (H_s / D_s)} + \frac{\rho_s D_s^2}{12} \left[\left(\frac{H_s}{D_s} \right)^2 - \frac{3}{16} \right] \cdot (\dot{\epsilon}^2 + \ddot{\epsilon}) + \frac{3}{64} \rho_s D_s^2 \ddot{\epsilon}, \quad (4)$$

where μ is the coefficient of Coulomb friction, and both H_s and D_s represent their respective instantaneous values. If the optimum value H_s / D_s is sought by setting, $\sigma_s^M - \sigma_s^C = 0$, then the following solution is obtained:

$$\left(\frac{H_s}{D_s} \right)_{\text{opt}} = - \left[\frac{2 \cdot \mu \sigma_s^M}{\rho_s D_s^2 \cdot (\dot{\epsilon}^2 + \ddot{\epsilon})} \right]^{1/3} \cdot \left[\left(1 - \sqrt{1 + \beta} \right)^{1/3} + \left(1 + \sqrt{1 + \beta} \right)^{1/3} \right],$$

and

$$\beta = \left(\frac{\rho_s D_s^2}{16 \cdot \mu \sigma_s^M} \right)^2 \cdot \frac{(\ddot{\epsilon} - 0.5 \dot{\epsilon})^3}{8 \cdot (\dot{\epsilon}^2 + \ddot{\epsilon})}. \quad (5)$$

While the detailed analysis of equations 4 and 5 can be found in reference (28), the major conclusions about the optimum specimen H_s / D_s ratio are summarized here. The optimum H_s / D_s is a function of coefficient of friction, specimen stress, density, strain rate, and strain acceleration. Thus, there is no universal optimum H_s / D_s ratio, rather it changes with $\dot{\epsilon}$ and $\ddot{\epsilon}$ of the test for a given specimen material. Based on the fact that the optimum H_s / D_s ratio is a function of σ_s^M / ρ_s of the specimen, Malinowski and Klepaczko (28) identified three ranges of optimum H_s / D_s values for metals:

1. For materials with high σ_s^M / ρ_s ratio (e.g., titanium, high-strength steel, etc.) – $1.0 \leq H_s / D_s \leq 1.5$.
2. For materials with medium σ_s^M / ρ_s ratio (e.g., aluminum, copper, etc.) – $0.5 \leq H_s / D_s \leq 1.0$.
3. For materials with low σ_s^M / ρ_s ratio (e.g., lead, gold, etc.) – $0.1 \leq H_s / D_s \leq 0.5$.

In addition to the previously mentioned discussion on the optimum H_s / D_s ratio for metallic specimens, there are additional guidelines for soft (29) and hard (27) specimens also.

Chen et al. (30) observed substantial wave attenuation in thick (0.25-in) RTV630 rubber samples

as compared with thin (0.06-in) samples, suggesting that depending on test temperature and specimen material, an H_s/D_s ratio of 0.25–0.50 can be used to minimize attenuation. Ceramic specimens, on the other hand, possess high-failure strength and relatively low-failure strain. In order to allow sufficient deformation of the specimen before failure, the recommended H_s/D_s ratio for ceramic specimens is usually higher than for the metallic specimens ($1.0 < H_s/D_s < 2.0$) (27).

1.1.2 Experimental Study on Specimen Shape and Failure

Harding (31) used waisted strip specimen (in-plane shape is rectangular and dog bone shaped through the thickness) under compression SHPB technique and found that stress equilibrium is hard to achieve. On the other hand, Harding's compression SHPB experiments on cylindrical specimens with specimen length to diameter ratio, $H_s/D_s = 1.0, 2.0$, and 2.5 in the warp and weft directions revealed that in addition to the shear band formation, specimens with higher H_s/D_s ratio introduce longitudinal splitting as an additional failure mode.

Takeda and Wan (32) tested unidirectional glass/polyester specimens with square cross section in the fiber direction and studied the evolution of specimen damage as a function of loading level controlled via a recovery SHPB. Figure 1 shows the damage at the impact end at three different load levels. Clearly, the stress concentration developed at the edges and corners of the specimen due to the nonplanar bar-specimen interface deformation initiated damage at those locations; and as the load is increased, the loci of failure progressed radially inward.

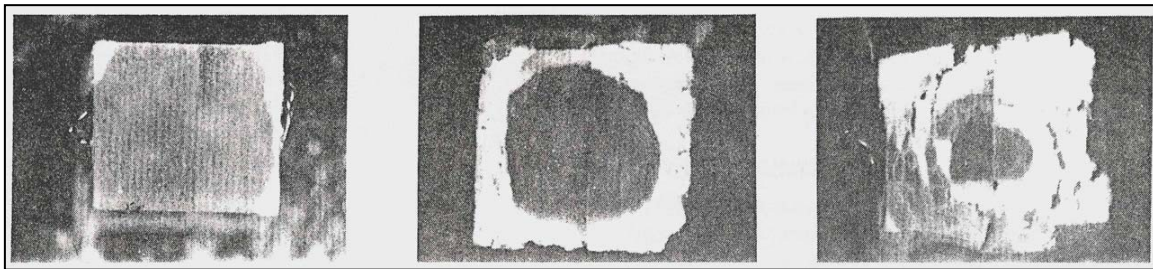


Figure 1. Damage at the impact end of Takeda's unidirectional specimen at different loading levels.*

Leber and Lifshitz (33) used dog bone-shaped hollow cylindrical specimens (figure 2) for torsional testing of plain-weave E-glass/epoxy composite materials; however, results from dynamic finite element analysis showed that the shear stress distribution is not uniform in the gage section of the specimen.

Deltort et al. (34) pointed out the importance of friction, elastic punching, and parasitic bending on the results of static and SHPB compression tests with standard cylindrical specimens in their brief article. They described that any imperfect contact between specimen and loading interfaces and the misalignment between the specimen and loading axes are the causes of specimen bending. Through quasi-static experiments and finite element modeling, they identified the fact

* Figure 1 is a reproduction taken from reference (32), figure 7, p 112.

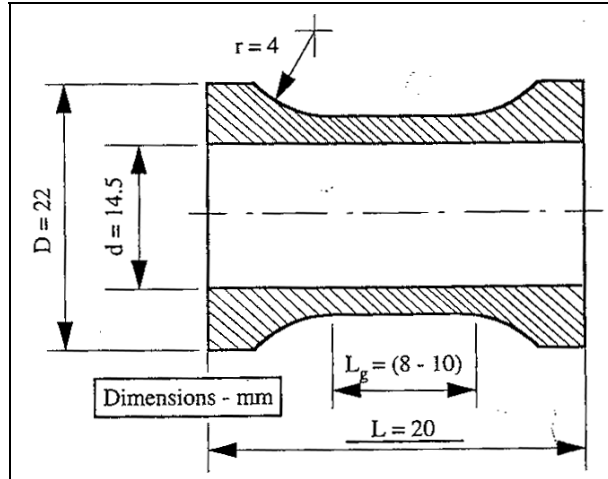


Figure 2. Dog bone-shaped hollow cylindrical specimen geometry for torsional testing.*

that friction between specimen and interfaces and elastic punching effect lead to a heterogeneous state of specimen strain and can cause barreling of the specimen at large deformation. A new specimen design is proposed, which has a dog bone/dumbbell shape (figure 3). They performed a few quasi-static and SHPB compression experiments to prove the concept. The new specimen is found to have a problem of buckling because of its longer length.

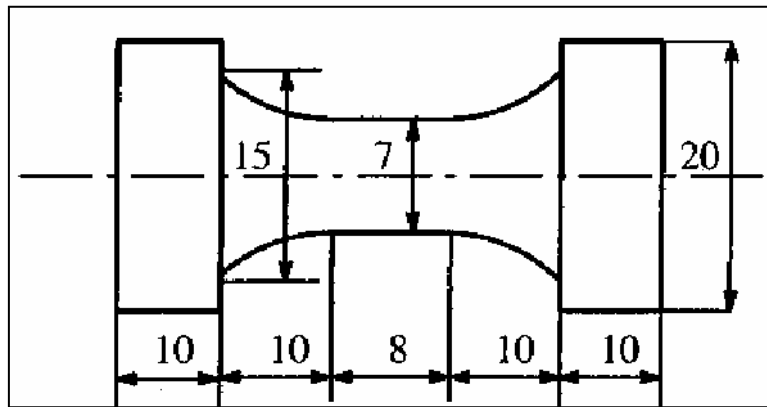


Figure 3. New compression SHPB specimen geometry proposed by Deltort et al.† All dimensions in millimeters.

Ninan et al. (35) used both two-dimensional (2-D) plane stress and an axisymmetric model of the full SHPB and studied the effect of interface friction and incident pulse shape. The strain history of a rectangular specimen (axial dimension smaller than bar diameter) was presented at five different points, considering both frictionless and constrained boundaries. The strain history/distribution was found uniform for the frictionless case, but nonuniform for the constrained case. A conclusion was made that friction at bar-specimen interfaces may produce nonhomogeneous strain distribution in the specimen.

*Figure 2 is a reproduction taken from reference (33), figure 3, p 394.

† Figure 3 is a reproduction taken from reference (34), figure 3, p C3-267.

1.2 Objectives

Earlier works considered the SHPB specimen design to minimize friction and inertia (radial and axial) through theoretical and numerical analyses. Bertholf and Karnes (36) described the first comprehensive 2-D numerical analysis of compression SHPB. A brief review of numerical Hopkinson Bar modeling can be found in reference (13). A more recent numerical study by Zencker and Clos (37) has identified that “in the initial state of a SHPB test, the specimen behaves elastically with high stress triaxiality. In this early phase, the results of the SHPB procedure are inaccurate. They can be improved by well-known inertia corrections, but error remains.” The objectives of the present study are different than what has been addressed by other researchers. In this study, specimen designs are presented which will improve the uni-axial stress state in the specimen in the elastic phase of deformation. In addition, the new experimental technique is presented which minimizes the planar bar-specimen interface deformation and thereby reduces the error in the measurement of average specimen strain using one-dimensional (1-D) Hopkinson bar analysis. New concepts of specimen and experiment designs are analyzed using a three-dimensional (3-D) finite element model of compression SHPB apparatus. All numerical simulations of compression SHPB experiment are performed using dynamic explicit Lagrangian hydrocode LS-DYNA 960.

2. Numerical Simulation of Compression SHPB Experiment

A traditional compression SHPB consists of two bars of equal length and diameter, and is known as incident/input bar (IB) and transmitter/output bar (TB). A striker bar (SB) impacts the impact end of the IB, while the specimen (S, SP) in the form of a right circular cylinder is sandwiched in between the IB and TB (figure 4a). The impact of a projectile produces a compression stress/strain pulse, which propagates along the bar and loads the specimen under compression. A part of the incident pulse reflects back from the incident bar-specimen (IB-S) interface and a part is transmitted to the TB through the specimen-transmitter bar (S-TB) interface. The incident ($\epsilon_i(t)$), reflected ($\epsilon_r(t)$), and transmitted ($\epsilon_t(t)$) pulses are recorded through the strain gages (SGs) mounted at the midlength on the bar surfaces, and are used to calculate the average stress and strain of the specimen following the 1-D Hopkinson Bar analysis (24).

In a previous study (13), a quartersymmetric finite element model of a compression SHPB was developed in three dimensions. A mesh sensitivity analysis along the length (Z-axis) was performed to identify the minimum number of elements necessary to obtain convergence, and 400 elements were found sufficient to predict the Hopkinson bar experimental responses. The accuracy of the numerical model was verified by simulating the 1-D stress wave propagation in a long rod with free and fixed boundary conditions. The contact modeling between bar-specimen and bar-bar interfaces was verified by computing the reflection coefficients from an interface with unequal cross sections. The impact-contact of an SB on the IB was verified by computing

the stress in the bar, particle velocities of the propagating stress waves, and the duration of pulses as a function of SB lengths. The finite diameter effect in an SHPB was evaluated by the study of shaped pulses. The model was also validated for a “bars together” calibration experiment. The model was found to predict all the previously mentioned analytical problems with sufficient accuracy. This well-verified and validated model is used in the present analyses. The axis of the cylindrical specimen is taken as the Z-axis, and the axis orthogonal to the Z-axis is taken as the radial axis, r (also X and Y axes [figure 4b]). The details of the model can be found in reference (13). For completeness, a brief summary is presented next.

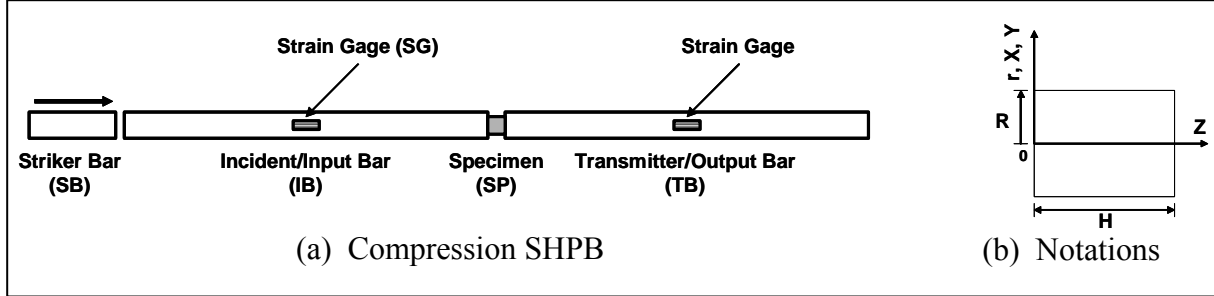


Figure 4. Schematic diagram of a compression SHPB and the notations used in the analyses.

A 3-D model of the SHPB is developed using 8-node solid elements. A 1-point integration scheme is used to save computational time. The longitudinal axis of the bars is taken as the geometric Z-axis. In the case of a specimen with a circular or rectangular cross section, two planes of symmetry passing through X-Z and Y-Z plane exist. In the present study, a quartersymmetric model (figure 5) with appropriate boundary conditions in the symmetric planes is used. The impact velocity of the SB is used as the initial condition, or a pressure pulse is applied on the impact face of the IB. A surface-to-surface contact interface condition without friction is defined between the bar interfaces. The specimen in the form of a right circular cylinder or a dog bone/dumbbell shape is considered.

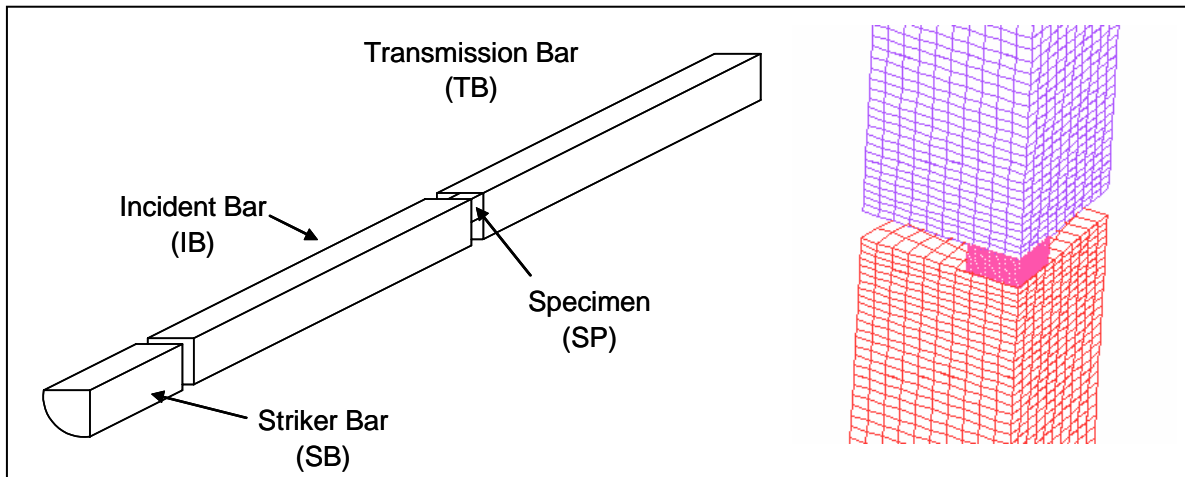


Figure 5. Quartersymmetric model of SHPB and finite element mesh.

The geometric dimensions of the model are presented in table 1; however, all of these dimensions can be varied as a test parameter. The bars remain elastic at all times during the SHPB experiment, and thus a linear-elastic isotropic material model is considered for the bars. The specimens are modeled with both linear-elastic and elastic-plastic isotropic material models. Two material parameters, Young's modulus (E) and Poisson's ratio (ν), are required to describe a linear-elastic model; however, two additional parameters, yield stress (σ_y) and tangent modulus (E_t), are necessary for elastic-plastic definition. For wave propagation analysis, density (ρ) of the material is also necessary. The material properties used in the numerical simulation are listed in table 2 including the calculated bar velocity $C_0 = \sqrt{E/\rho}$.

Table 1. Geometric properties of the SHPB.

Parameter	SB	IB	TB	SP
Length (mm)	304.80	1524	1524	Variable
Diameter (mm)	25.40	25.40	25.40	Variable

Table 2. Linear-elastic and elastic-plastic material constants.

Material	P (g/cm ³)	E (GPa)	ν	σ_y (MPa)	E_t (MPa)	c_0 (m/s)
Inconel ^a	8.40	201.33	0.290	—	—	4895.70
Steel	7.85	206.91	0.300	830.00	0.0	5134.00
Aluminum	2.70	68.95	0.285	249.00	840.00	5053.42
Ceramic	3.95	370.00	0.220	—	—	9678.37

^aInconel is a registered trademark of the INCO family of companies.

In the SHPB experiment, the most common measured quantities are the impact velocity of the projectile, axial strain on the bar surface as a function of time via surface mounted SGs, and the axial and transverse strains on the specimen surface as a function of time. In the numerical experiment, displacement and velocity of nodes, strain and stress of the elements, interface forces, and material and global energies can be investigated as a function of time. Time history data of selected nodes, elements, and interfaces of interest are stored during solution and analyzed during the postprocessing phase. The validated model, as described in reference (13), is then used for detailed numerical analyses.

In order to enforce a known boundary condition, a parametric stress pulse is taken as the input to the impact face of the IB with four parameters: t_A , t_B , t_C , and P_{max} (figure 6). By suitable choice of these parameters: different pulse shapes can be obtained (e.g., rectangular, trapezoidal, and triangular). Detail parameters used in a numerical experiment will be described in each different case study.

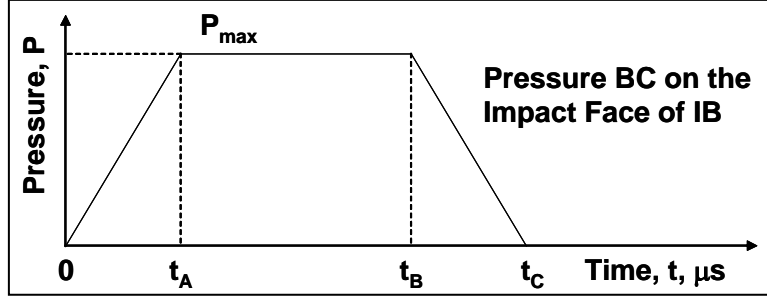


Figure 6. Loading history on the impact face of the IB.

3. Effect of Nonplanar Bar-Specimen Interface: The Problem

It is well known that the particle velocity of the free end of a long bar is twice the particle velocity of the propagating pulse, and that of a built-in end is zero. Figure 7 shows the schematic of a cylindrical specimen sandwiched between IB and TB. Clearly, if the specimen diameter is smaller than that of the bars, and the acoustic impedance of the specimen is comparable with that of the bars, then the particle velocity of the free surface ($R_s < r < R_B$) will be higher than that of the interface where the bar and the specimen is in contact ($0 < r < R_s$). In this case, the radial distribution of axial deformation, $u_i^j(r)$, of the IB-S and S-TB interfaces is not uniform, i.e., the bar-specimen interfaces undergo a nonplanar deformation (12, 13).

It has been shown (13) that this nonplanar deformation of the IB-S interface produces an average displacement of the specimen at this interface, which is smaller than the average displacement of the IB edge at the IB-S interface. Similar argument can be made for the S-TB interface deformation also. Thus, the average strain of the specimen measured from the reflected pulse is always higher than the actual strain in the specimen (13). Because the deformation of the bar-specimen interfaces is nonplanar, in the elastic phase of deformation, the nonuniform radial displacement field on the specimen in the bar-specimen interfaces produces a nonuniform distribution of axial stress along the length of the specimen, which can be measured by measuring the axial stress along the length on the surface of the specimen (13). This nonplanar interface deformation can cause barreling of the specimen. Thus, in the elastic deformation phase of a smaller diameter hard specimen (e.g., composites in the fiber directions, and ceramics as compared to metallic bars), two important assumptions of 1-D Hopkinson bar analysis (i.e., [a] bar-specimen interfaces remain planar and [b] specimen is under uni-axial stress state) fail to hold true. However, in the plastic phase of deformation, the specimen is found to achieve uni-axial stress state along the length, which is the outcome of radial outward plastic flow of materials under axial compression.

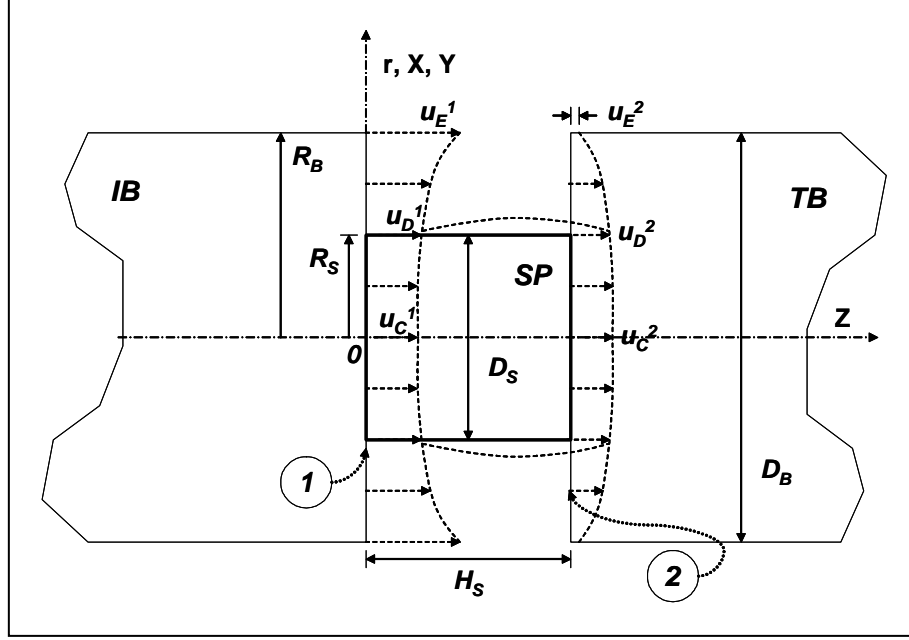


Figure 7. Nonplanar bar-specimen interface deformation model of a small diameter hard specimen: u_i^j – axial displacements in Z-direction; subscripts $i = C, D$, and E represent bar-center, specimen-edge, and bar-edge, respectively; superscripts $j = 1$ and 2 ; “1” = IB-S interface; “2” = S-TB interface.*

The nonplanar deformation of bar-specimen interface is related with the nonuniform axial stress distribution in the specimen. To correct this problem, one can design a new experiment such that the bar-specimen interface remains plane at all time during dynamic deformation of the specimen, or can design a specimen such that the axial stress distribution in the specimen is uniform. In the following sections, new specimen and experiment design is presented, which improves the uni-axial stress distribution in the specimen and provides better planar bar-specimen interface conditions.

4. Uni-Axial Stress Along the Specimen Through Specimen Design: Partial Solution

The nonplanar deformation of the bar-specimen interfaces is identified as the main reason for nonuniform axial stress distribution along the length of the specimens. A numerical simulation with a cylindrical ceramic specimen of specimen diameter to bar diameter ratio, $D_S/D_B = 0.60$, and specimen length to specimen diameter ratio, $H_S/D_S = 1.00$, which is equivalent to the dimensionless specimen length, $\hat{D}_S = (D_S/D_B)/(H_S/D_S) = D_S^2/(D_B \cdot H_S) = 0.60$, has been

* Adapted from references (12) and (13).

performed with a triangular input stress pulse ($t_A = 99 \mu s$, $t_B = 101 \mu s$, $t_C = 200 \mu s$, and $P_{max} = 500 \text{ MPa}$); parameters are described in figure 6 of duration $T = 200 \mu s$. Detailed results of this simulation are presented in reference (13). The IB and TB ($D_B = 25.4 \text{ mm}$) considered in this simulation were made from steel (see table 2 for properties). The cross section of the bar is modeled with 195 elements, and the specimen cross-section has one-to-one node connectivity for stable contact modeling. The incident, reflected and transmitted stress in the bars, is presented in figure 8a as dotted lines with open symbols. It is clear from figure 8a that the specimen is loaded under compression during the first half of the incident pulse ($0 < t/T < 0.50$), and the second half of the pulse represents unloading ($0.50 < t/T < 1.00$). Figure 9a shows the contours of stress distribution in the specimen at three different times ($t/T = 0.15, 0.30, 0.45$) during the ramp-loading phase. The stress amplitude is highest at time, $t/T = 0.45$, and the stress concentration is visible at the edges of the specimen. A similar profile is also obtained by Anderson et al. (38) while modeling the compression of cylindrical specimen with truncated cones as loading block in the SHPB setting. Figure 9 also shows that the stress on the free surfaces ($R_S < r < R_B$) of the bar-specimen interfaces is zero.

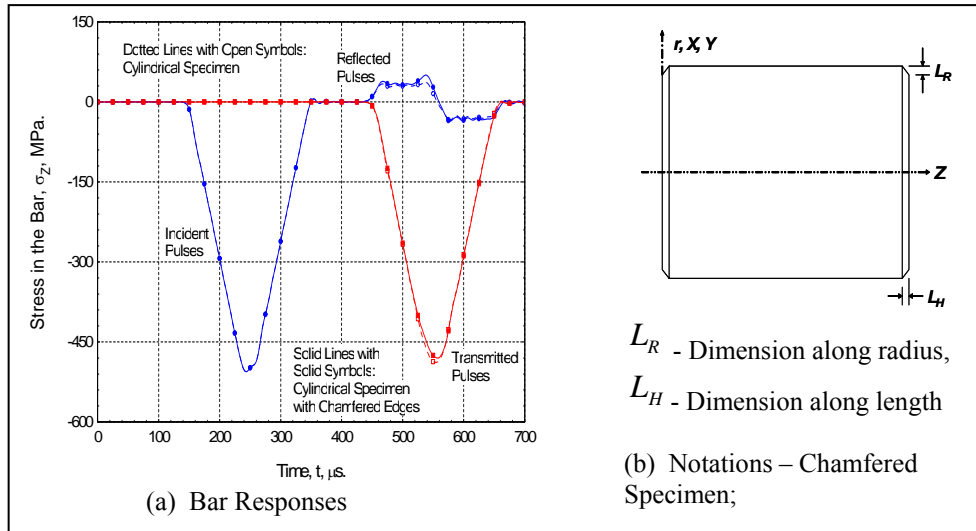


Figure 8. Numerical Hopkinson bar responses for two different test cases.

4.1 Specimen Design 1: Cylindrical Specimen With Chamfered Edges

The nonplanar deformation model presented in figure 7 suggests that a specimen with curved loading faces can eliminate the nonuniform axial stress distribution in the specimen. While the shape of the curve to which the specimen loading surfaces should be machined can be determined by solving the nonlinear contact problem, it is obvious that this solution process is extensive in nature. To demonstrate the concept, a cylindrical specimen with chamfered edges is considered instead (figure 8b). The finite element model of this chamfered specimen is presented in figure 10. The geometry of the chamfer can be described by two variables, L_R and L_H , as shown in figure 8b.

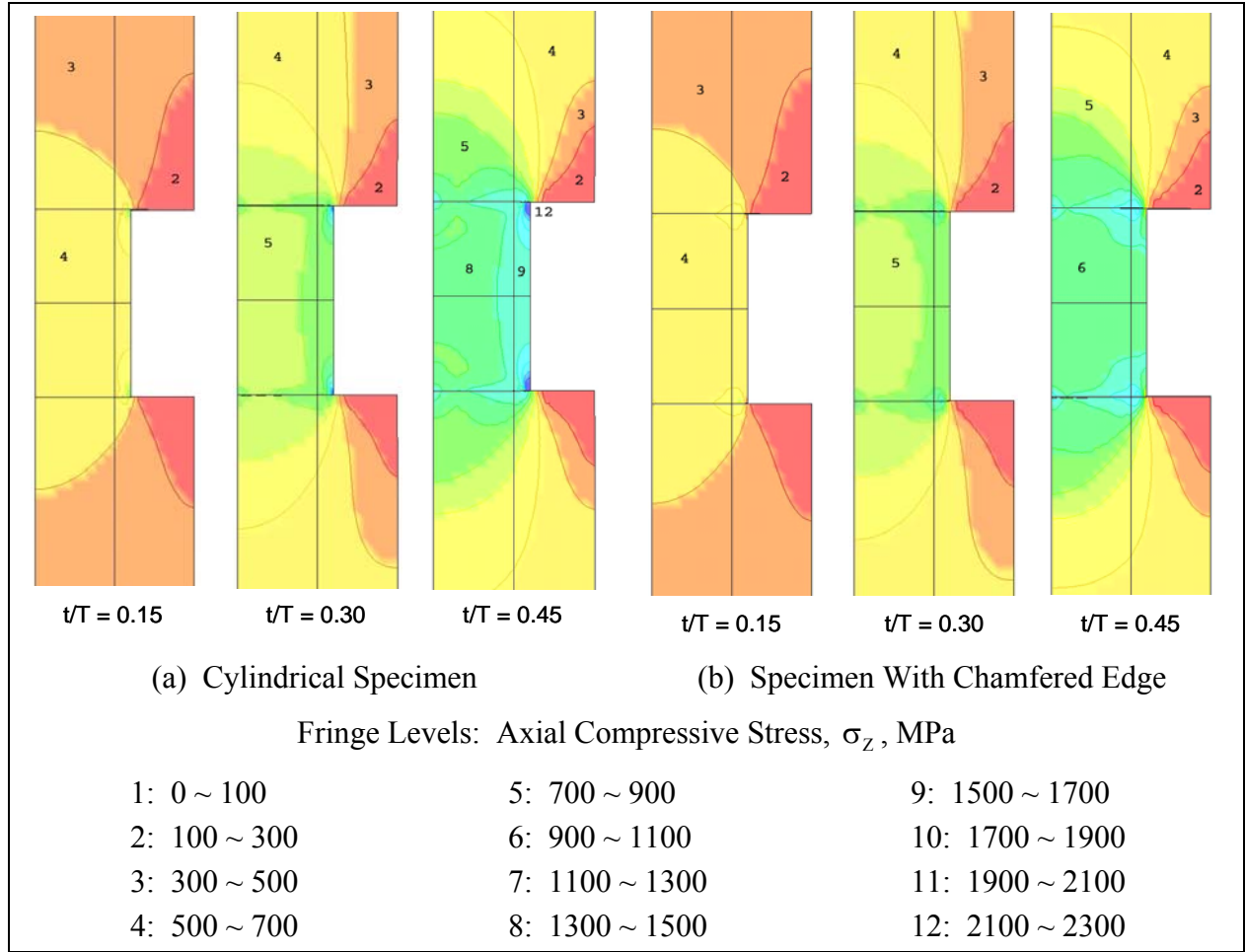


Figure 9. Contours of axial stress distribution in the specimen at a different time.

The numerical model of the chamfered specimen is loaded with the same boundary condition as in the case of a pure cylindrical specimen. The reflected and transmitted stresses in the bars (figure 8a, solid lines with solid symbols) appear to be a little different than the case of a cylindrical specimen. The contour of axial stresses at different times in the case of the specimen with chamfered edges (figure 9b) appears to be more uniform than the cylindrical specimen. It has been shown in reference (13) that the uniformity of the distribution of the axial stress in the specimen along the length can be represented by plotting the axial stresses on the surface of the specimen along the length as a function of time (figure 11a). In the elastic phase of deformation, the axial stress distribution on the surface of cylindrical specimen is found to be nonuniform at all time. The axial stress near the bar-specimen contact interfaces is higher than the midlength of the specimen, and the distribution has an elliptical shape. The distribution of axial stresses on the surface of a cylindrical specimen with chamfered edges is shown in figure 11b. As expected, the stress distribution on the surface of the specimen is almost uniform along the length of the specimen, except at the chamfered edges. At the chamfered edges, there are additional free

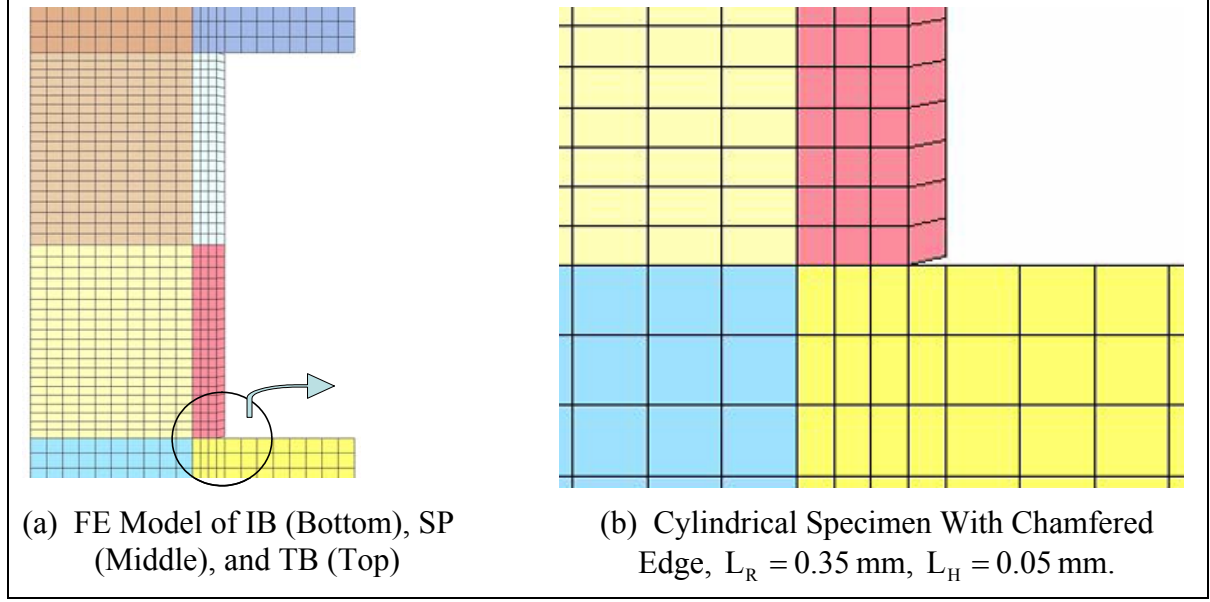


Figure 10. Quartersymmetric finite element model of Hopkinson bars and cylindrical ceramic specimen with chamfered edges, $D_S / D_B = 0.60$, $H_S / D_S = 1.00$, $\hat{D}_S = 0.60$.

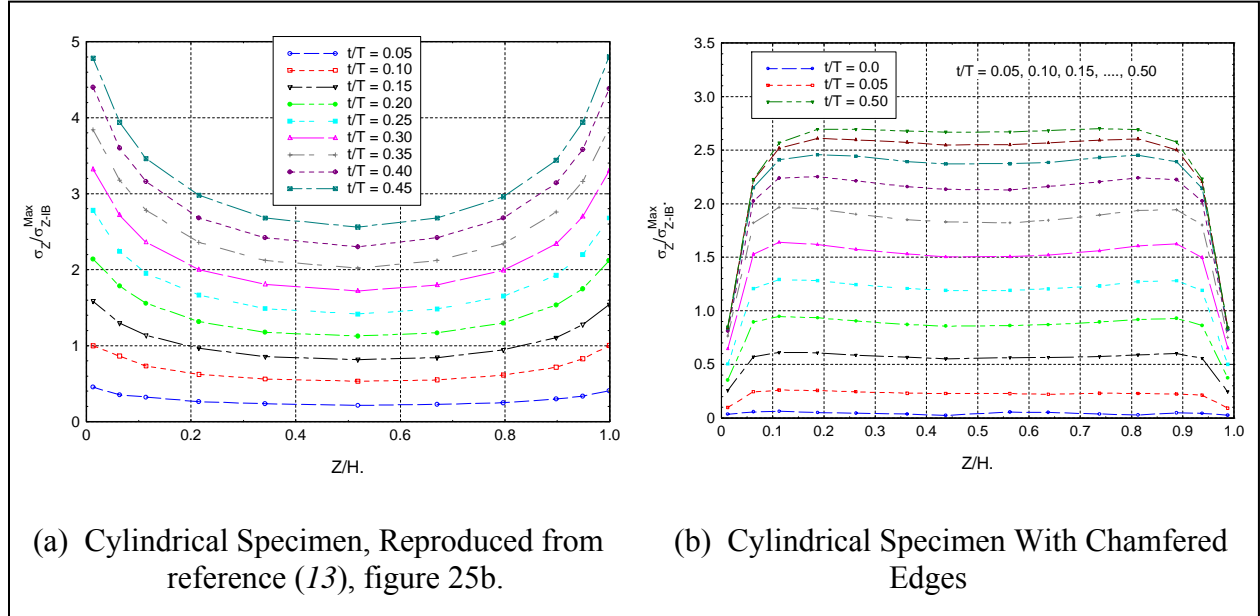


Figure 11. Axial stress distribution on the surface of ceramic specimen at a different time, $\hat{t} = t / T$, $\hat{D}_S = 0.60$, $r / R = 1.00$, $\sigma_{Z-IB}^{\text{Max}} = P_{\text{max}} = 500$ MPa.

surfaces, on which normal stress components are zero. This study shows that by simply making chamfered edges on both sides of the specimen, it is possible to obtain uniform axial stress condition in the elastic deformation phase.

In reference (13), it has been shown that the nonuniform distribution of axial stress on the surface of cylindrical specimen has self-similar behavior under ramp loading in the elastic phase of deformation, which can be shown by normalizing the axial stress by that at the midlength of the specimen (figure 12). In figure 12, the self-similar behavior of axial stress on the surface of a cylindrical specimen with chamfered edges is also presented. This figure shows the benefit of a chamfered specimen in attaining the uniform stress distribution in most part of a cylindrical specimen.

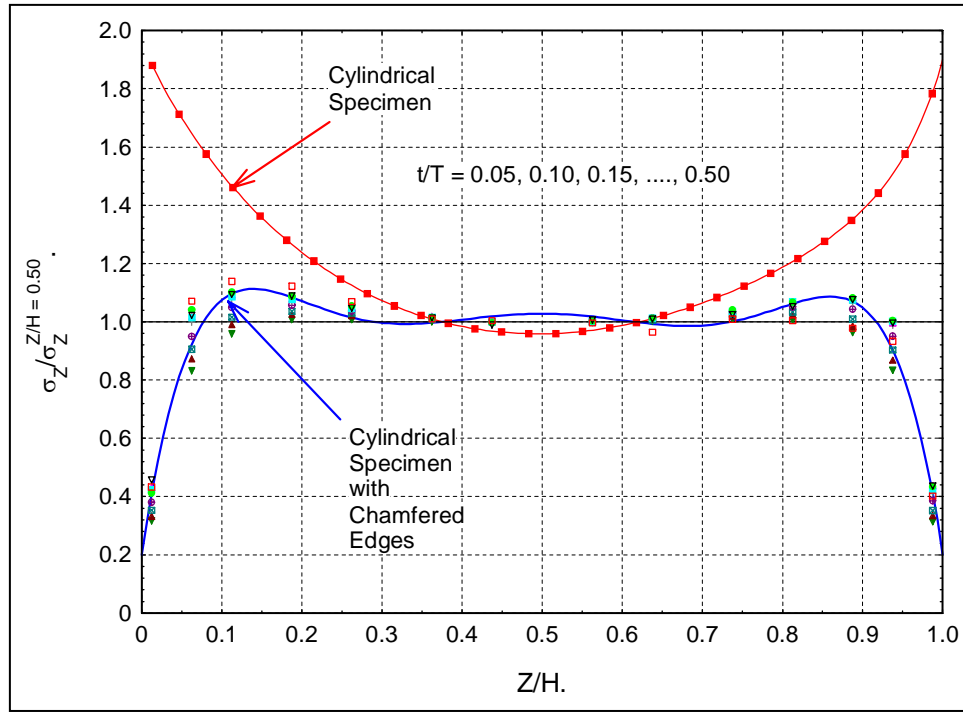


Figure 12. Distribution of dimensionless axial stress along the length of a cylindrical specimen with and without chamfered edges.

The axial stress distribution along the radial direction of the specimen at different Z / H locations of a cylindrical specimen at time $\hat{t} = t / T = 0.25$ is presented in figure 13. In figure 13a, the axial stress is normalized with the maximum axial stress in the incident pulse.

The axial stress distribution in the radial direction is almost uniform in the range, $0.10 < Z / H < 0.90$, which is also evident from figure 12. In figure 13b, the axial stress is normalized with the axial stress at location $r / R = 0.025$ and plotted as a map along the length of the specimen. This figure clearly shows that the axial stress distribution is uniform over the specimen length except for a small region around the chamfered edged. It has been shown in reference (13) that the uniform distribution of axial stress on the surface of a cylindrical specimen along the length guarantees the overall uniformity of axial stress in the specimen (in the plastic deformation phase). Figure 13 proves the validity of that general statement in the

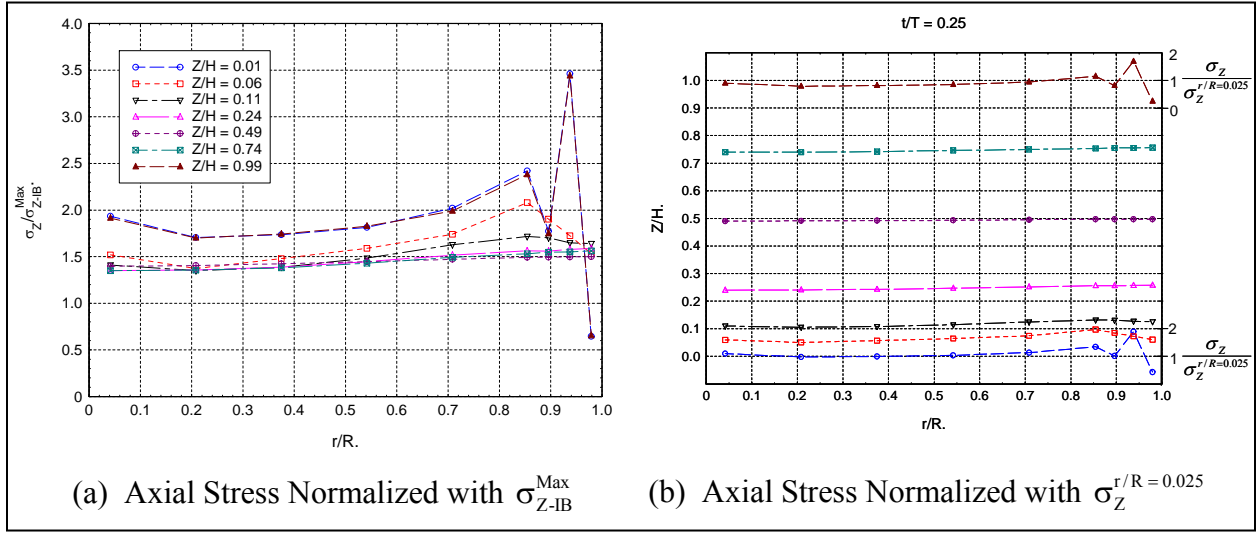


Figure 13. Distribution of axial stress in the radial direction at different Z/H locations of a cylindrical specimen with chamfered edges, $\hat{t} = t/T = 0.25$.

elastic deformation phase in case of a cylindrical specimen with chamfered edges. Chamfering the edges of the specimen can thus effectively minimize the problem of nonuniform axial stress distribution of a small diameter cylindrical specimen. The analysis of the dog bone/dumbbell-shaped specimen design suggested by Deltort et al. (34) is presented next.

4.2 Specimen Design 2: Dog Bone/Dumbbell-Shaped Cylindrical Specimen

One can analyze the distribution of axial stress on the surface of a cylindrical specimen in the elastic deformation phase (figure 12) and can heuristically make a hypothesis that a traditional dog bone/dumbbell shape cylindrical specimen can also provide uniform axial stress distribution on the surface of the specimen in the gage section. It is also obvious that a specimen with a diameter equal to the bar minimizes the nonplanar deformation of the bar-specimen interfaces (12, 13). The cylindrical dog bone/dumbbell-shaped specimen proposed by Deltort et al. (34) also considered the end of the specimen to be of equal diameter to the bars. This specimen and associated parameters to define the specimen geometry are presented in figure 14. Two important parameters of the dog bone specimen are the length of the right circular cylinder part at the specimen ends, L_F , (which will be in contact with the bars), and the length of the parabolic section, L_C , of the specimen. The length of the cylindrical gage section is denoted by usual nomenclature, H_S .

To be consistent with our analyses of cylindrical specimens with and without chamfered edges, the specimen dimensionless parameters are kept unchanged (i.e., $D_S / D_B = 0.60$, $H_S / D_S = 1.00$, $\hat{D}_S = 0.60$). Because the specimen aspect ratio is taken as $H_S / D_S = 1.00$, the total length of the dog bone-shaped specimen is longer than the cylindrical specimens.

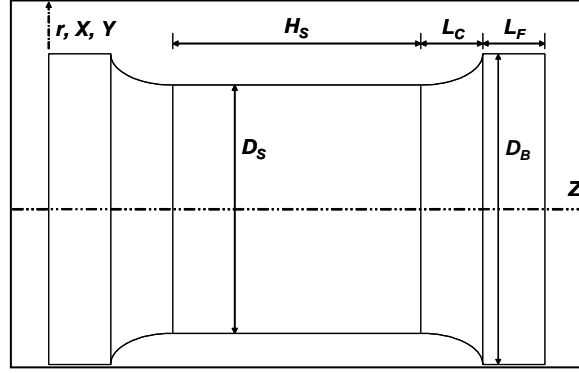


Figure 14. The parametric definition of a cylindrical dog bone/dumbbell-shaped specimen proposed by Deltort et al. (34).

A finite element model of the dog bone-shaped specimen is developed by keeping the same strategy of one-to-one correspondence of nodes between the contact interfaces and is presented in figure 15a. Both the bar and specimen cross-section is modeled using 144 elements. The specimen parameters have been marked on the FE model, and the different sections and interfaces are highlighted. Similar loads and boundary conditions are used as in the case of specimen design 1. Figure 15b shows the contour of axial stress distribution in the dog bone-shaped specimen at three different times, as is also presented in previous cases (figure 9). The range of fringes is also the same for comparison with figure 9. The axial stress distribution of the dog bone-shaped specimen is superior to that of the cylindrical specimen with chamfered edges. The distribution of axial stress on the surface of the dog bone-shaped specimen along the length is presented in figure 16, where the Z -coordinate at the beginning of the gage section is taken as zero to make a comparison with the cylindrical specimens. The results for cylindrical specimens with and without chamfer are also plotted for comparison. There still remains some nonhomogenous distribution of axial stress at the beginning of the gage section; however, the overall distribution is superior to that of the cylindrical specimen with the chamfered edge.

A dog bone-shaped shaped cylindrical specimen can provide a uni-axial stress condition in the specimen in the elastic deformation phase; however, the calculation of the specimen average strain from bar responses becomes problematic due to the presence of the additional length of the specimen in addition to the gage section. However, because the specimen has uni-axial stress state over the gage length, SGs can be mounted on the surface of the specimen to measure the specimen strain, which is also true for the case of the cylindrical specimen with chamfered edges. It is interesting to note that, in testing of ceramic materials, SGs are used on the specimen to measure the specimen strain along with shaped pulses (27). However, uncertainty remains in selecting an SG of specific gage length for a specific specimen length, even if one decides to bond the SG in the midlength of the specimen. From the present analysis, a major conclusion

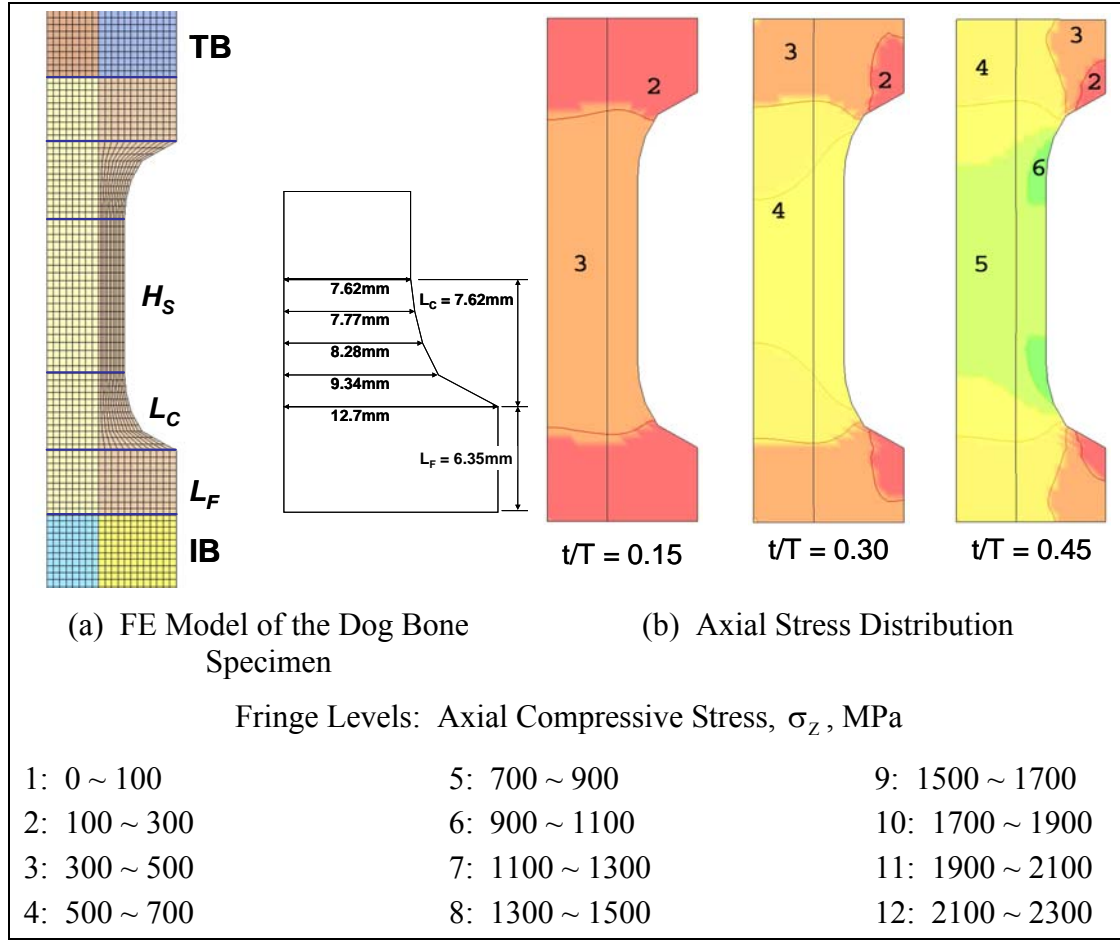


Figure 15. Contours of axial stress distribution in the dog bone-shaped specimen at a different time.

can be made that Hopkinson Bar testing of linear-elastic materials (e.g., composites in fiber direction and ceramics) can be performed while satisfying the uni-axial stress condition in the elastic phase of deformation if a chamfered or dog bone-shaped specimen is used. The other conclusion is that one can use SG to measure specimen strain with confidence, knowing the fact that the specimen is under uni-axial stress state in case of a chamfered and a dog bone/dumbbell-shaped specimen.

Both of the specimen designs have their own limitations. The chamfered cylindrical specimen does not guarantee the planar bar interface condition, and thus the solution is not complete. The dog bone-shaped specimen having equal diameter guarantees planar bar-specimen condition, however, requires an additional SG to measure the strain in the specimen. It is also important that the specimen remains under stress equilibrium. The deviation of stress equilibrium in the specimen is usually characterized by the factor $R = \Delta\sigma / \sigma_{avg} = 2 \cdot (F_1 - F_2) / (F_1 + F_2)$ (12, 13) and is presented in figure 17 for all three cases. The forces, F_1 and F_2 , at the IB-S and S-TB interfaces, are taken from the time history of contact forces at the corresponding interfaces.

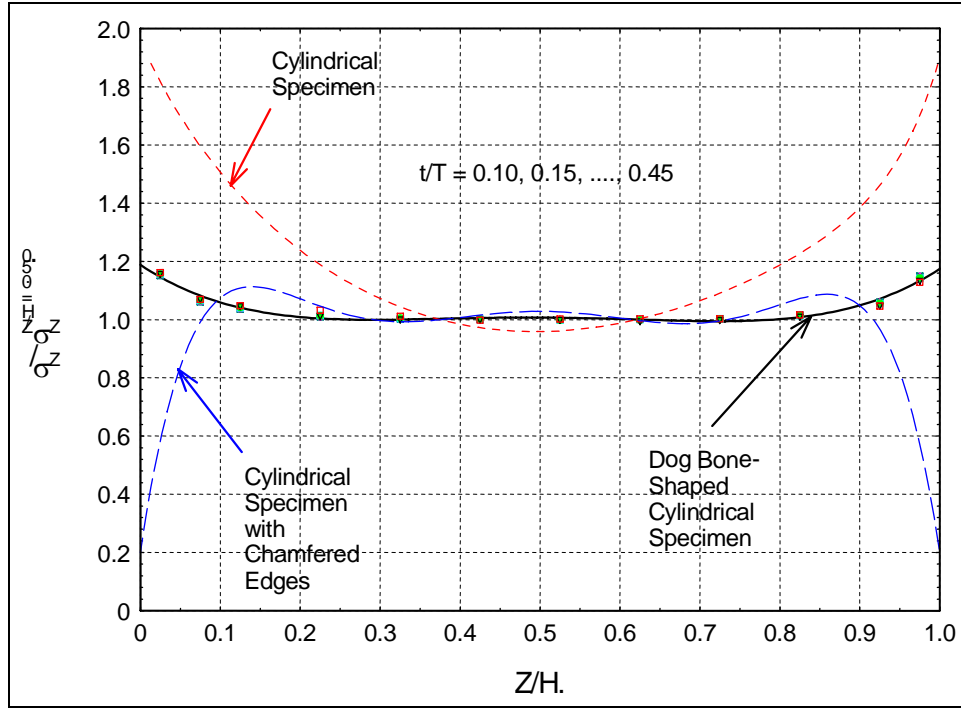


Figure 16. Distribution of dimensionless axial stress along the length of a dog bone-shaped specimen and that for cylindrical specimens with and without chamfered edges.

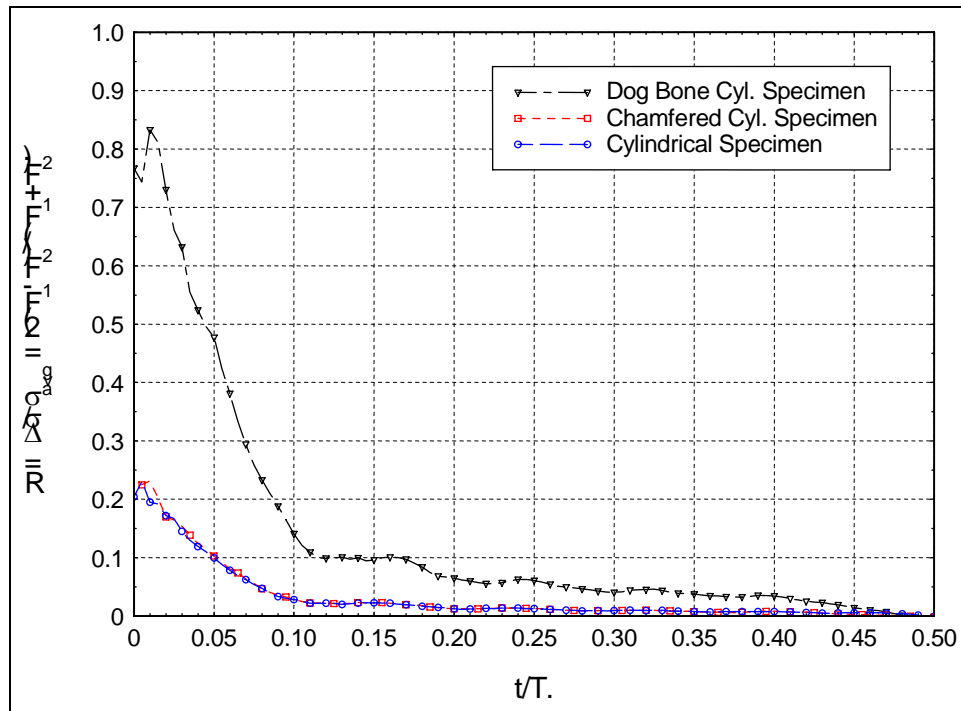


Figure 17. Deviation from stress equilibrium of different specimen designs.

It has been shown by the authors (13) that the specimen is not under stress equilibrium at anytime as can also be seen from figure 17. It is interesting that the cylindrical specimen with chamfered edges does not provide any better stress equilibrium for the specimen. However, the dog bone/dumbbell shaped specimen, being longer in length, has the deviation from equilibrium, which is much higher than the cylindrical specimens with chamfered edges. In both the cases, additional considerations should be undertaken to improve the stress equilibrium in the specimen. In separate works (39, 40), analytical techniques have been proposed to address the issues related to deviation of stress equilibrium. However, in general, better stress equilibrium can be achieved by using thinner specimens (12).

5. Planar Bar-Specimen Interface Condition Through Experiment Design: Complete Solution

The nonplanar deformation model of a small diameter hard specimen is presented in figure 7 and is also discussed in references (12, 13, 34). The main reason for the nonplanar deformation of the bar-specimen interface is that the free end of the IB, which is not in contact with the specimen ($R_S < r < R_B$), moves with higher particle velocity than the portion in contact with the specimen ($0 < r < R_S$), as described in figure 7. If one uses a specimen with diameter equal to the bar ($D_S = D_B$), the bar-specimen interfaces will remain planar. However, if high strain rate stress-strain diagram up to the failure of the specimen is sought, a realistic engineering practice is to use a small diameter specimen such that the stress level in the specimen is sufficiently high to cause damage or failure. If a smaller diameter specimen is used, ideally one can use a hollow cylindrical tube to load the free end of the specimen. In that case, the transmitter bar diameter should be equal to the specimen diameter to support the specimen on the transmission end. A new compression SHPB experimental technique is proposed in this report for the first time to guarantee the planar bar-specimen interface condition, and is presented in figure 18.

5.1 Compression SHPB With a TT

The new compression SHPB has several unique features, which include a transmitter /transmission bar (TB) that is equal to the SP diameter, or a little greater diameter than the specimen to accommodate the radial expansion due to Poisson's effect. It has a TT with an inner diameter a little greater than the TB, such that the TB can have a sliding fit inside the TT; and the outer diameter of the TT is equal to the diameter of the IB. The length of the TT should be more than $4\times$ the SB length, and should be approximately half the length of the TB. Independent SGs should be mounted on the IB, TT, and TB. Figure 18 shows that both the specimen and the TT are in contact with the IB. When the incident pulse reaches the IB-S/IB-TT interface, a part of it is transmitted to the TT and a part to the specimen. If the TT and the IB are made from the same material, the reflection coefficient of the area of IB that is in contact with the TT is zero (acoustic impedance of the IB and TT tube being the same, i.e., $Z_{IB} = \rho_{IB}c_{0IB} = \rho_{TT}c_{0TT} = Z_{TT}$).

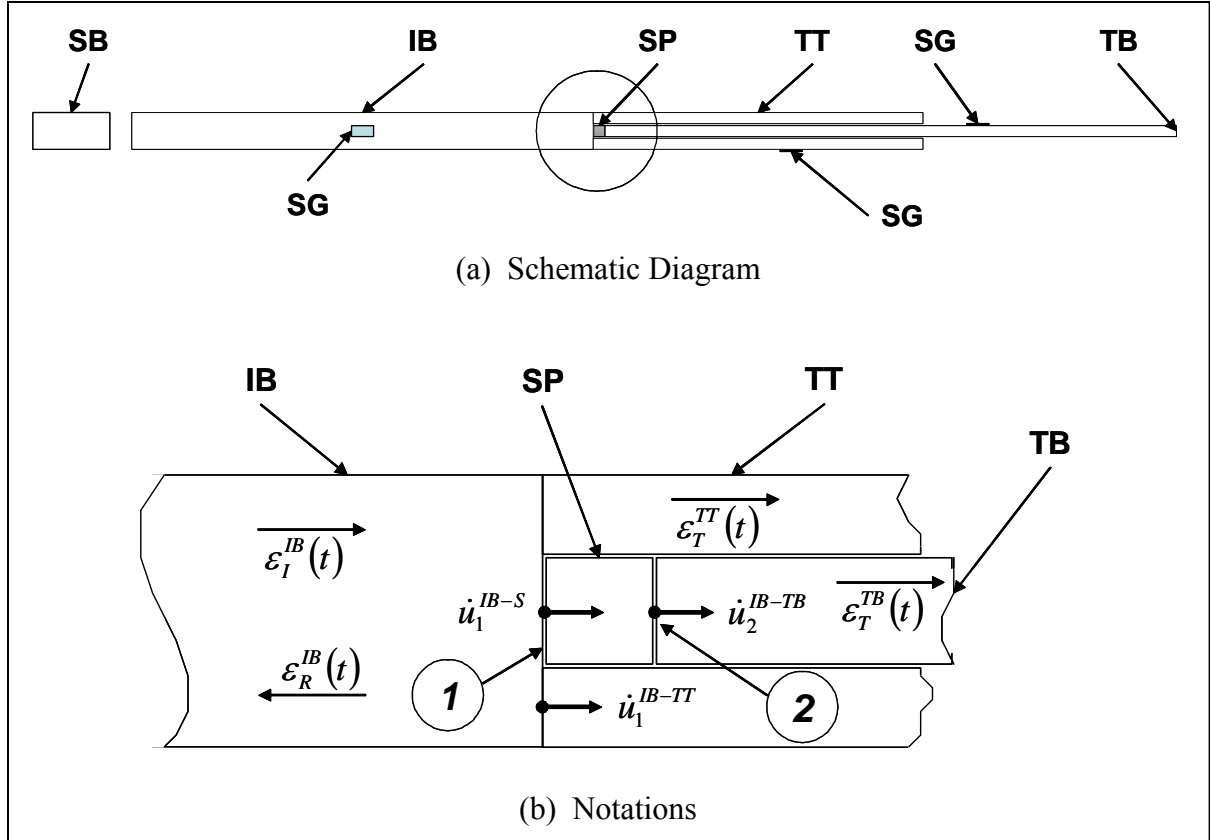


Figure 18. A new compression SHPB experimental set-up with TT.

The reflection coefficient of the part of IB that is in contact with the specimen depends on the impedance of the specimen. If the impedance of the specimen is 50% of the bar, then the reflection coefficient of the IB-S contact area is $-\frac{1}{3}$ (negative one-third), and if it is 50% more than the bar, then the reflection coefficient is $+\frac{1}{5}$ (positive one-fifth). Because the reflection from the IB-TT interface is zero, the reflected pulse recorded by the SG mounted on the IB surface will consist only of the reflections from the IB-S contact interface and from the free surface of the IB if there is any clearance between the specimen and the TT. Thus, the particle velocities at IB-S and IB-TT interfaces can be expressed as

$$\dot{u}_1^{IB-S} = -c_{0IB} \times [\epsilon_I^{IB}(t) - \epsilon_R^{IB}(t)] \quad (6)$$

and

$$\dot{u}_1^{IB-TT} = -c_{0IB} \times \epsilon_I^{IB}(t) = -c_{0TT} \times \epsilon_T^{TT}(t), \quad (7)$$

and the corresponding displacements as

$$u_1^{IB-S} = -c_{0IB} \cdot \int_0^t [\epsilon_I^{IB}(t) - \epsilon_R^{IB}(t)] \cdot dt \quad (8)$$

and

$$u_1^{\text{IB-TT}} = -c_{0\text{IB}} \cdot \int \varepsilon_1^{\text{IB}}(t) \cdot dt = -c_{0\text{TT}} \cdot \int \varepsilon_T^{\text{TT}}(t) \cdot dt, \quad (9)$$

where subscript 1 represents the IB-S/IB-TT interface, and the superscripts denote the location where the properties are measured at. If the IB-S/IB-TT interface remains planar then the following equity should exist:

$$u_1^{\text{IB-S}} = u_1^{\text{IB-TT}}. \quad (10)$$

If this equity exists, then either of equations 8 or 9 can be taken as the displacement of the IB-S/IB-TT interface, otherwise one can take an algebraic average as the displacement at this interface:

$$u_1^{\text{IB-S/IB-TT}} = (u_1^{\text{IB-TT}} + u_1^{\text{IB-S}})/2. \quad (11)$$

A complex stress wave reverberation in the specimen takes place, and the stress wave is transmitted to the TB. The particle velocity and displacement at the S-TB interface can then be expressed as

$$\dot{u}_2^{\text{S-TB}} = -c_{0\text{TB}} \cdot \varepsilon_T^{\text{TB}}(t) \quad (12)$$

and

$$u_2^{\text{S-TB}} = -c_{0\text{TB}} \cdot \int \varepsilon_T^{\text{TB}}(t) \cdot dt, \quad (13)$$

where subscript 2 represents the S-TB interface.

It is well known that the stress wave propagation in finite diameter bars is dispersive (3, 41), and thus a dispersion correction of the strain signals recorded on IB, TT, and TB should be performed (10, 12). It is important to mention that the dispersion correction methodology automatically performs the time sifting of incident, reflected and transmitted pulses to a common zero, and makes the algebraic manipulation easy. Once the dispersion correction procedure is performed, the average strain of the specimen can be expressed as

$$\varepsilon_s(t) = (u_2^{\text{S-TB}} - u_1^{\text{IB-S/IB-TT}})/H_s. \quad (14)$$

Because the free end of the IB-S interface is loaded with the TT and the TB diameter is equal to the specimen diameter, it is anticipated that the bar-specimen interfaces will remain planar at all time. Thus the major problem of nonplanar bar-specimen interface condition of a smaller diameter hard specimen can be resolved by the new compression SHPB with TT.

Following the 1-D stress wave propagation assumptions (12), the forces in the IB-S/IB-TT interface and S-TB interface can be expressed as

$$F_1(t) = A_{\text{IB}} E_{\text{IB}} [\varepsilon_1^{\text{IB}}(t) + \varepsilon_R^{\text{IB}}(t)] - A_{\text{TT}} E_{\text{TT}} \varepsilon_T^{\text{TT}}(t), \quad (15)$$

and

$$F_2(t) = A_{TB} E_{TB} \epsilon_T^{TB}(t) . \quad (16)$$

The average stress in the specimen then can be expressed as

$$\sigma_s(t) = [F_1(t) + F_2(t)] / 2 \cdot A_s , \quad (17)$$

which is equivalent to the “3-wave” analysis as described by Gray (24). Because equation (17) use four different measured strains to calculate the average specimen stress, this analysis can be termed as “4-wave” analysis.

The use of a TT is reported in literature by Harding and Huddart (21) in the dynamic punch shear testing technique, and by Nemat-Nasser et al. (8) in the tri-axial Hopkinson bar test technique. However, the unique use of TT to guarantee the planar bar-specimen interface condition is reported in this report for the first time. The numerical experiment of this new SHPB design is presented next to provide the proof of concept and validity of analysis.

5.2 Numerical Simulation of Compression SHPB With TT

The cross section of the specimen and the TB is modeled with 280 and 300 elements, respectively; while the IB and TT cross sections are modeled with 540 and 240 elements, respectively. Along the length of the IB and TB, 400 elements are used as described for the earlier case; however, 200 elements along the length of TT are used. A specimen with chamfered edges is used in this model, which guarantees the uni-axial stress along the length of the specimen. The parameters of the chamfered specimen are the same as described earlier. Figure 19 shows the FE model at the bar-specimen interfaces location. Properties of steel are used to model the bars, and the specimen is modeled with elastic-plastic aluminum and elastic ceramic materials.

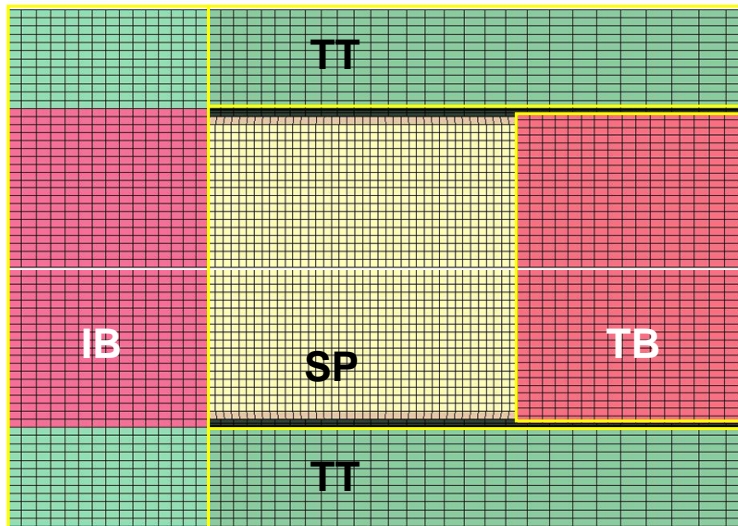


Figure 19. Finite element model of the compression SHPB with TT.

The geometric dimensions of the SHPB with TT model are as follows: $L_{IB} = 1524$ mm, $D_{IB} = 25.4$ mm, $L_{TT} = 562$ mm, $D_{TT}^{ID} = 15.875$ mm, $D_{TT}^{OD} = 25.4$ mm, $L_{TB} = 1524$ mm, $D_{TB} = 15.1$ mm, $H_s = 15.24$ mm, and $D_s = 15.1$ mm. These dimensions for the bars and the specimen represent a realistic experiment, where the specimen diameter is a little less than the TB, and the diameter of the TB is also a little less than the inner diameter of the TT. A triangular input stress pulse ($t_A = 99 \mu s$, $t_B = 101 \mu s$, $t_C = 200 \mu s$, and $P_{max} = 500$ MPa) of duration $T = 200 \mu s$ is used at the impact end of the projectile. The bar responses (element stresses on the bar surface at midlength) are presented in figure 20 with aluminum and ceramic specimens for the IB, TB, and TT. Note that the reflected and transmitted pulses measured at midlength of the IB and TB have the same time references; however, the transmitted pulse measured at midlength of the TT appears early in time because the length of TT is half of the IB. In the case of the aluminum specimen, a reflected pulse with a nearly constant amplitude up to $500 \mu s$ represents the elastic deformation phase, and the increase in amplitude after that represents the plastic deformation, which is also evident from the transmitted pulse. However, for the ceramic specimen, the reflected pulse has near zero amplitude because the impedance ratio of steel and ceramic is 1.054. As described earlier, the stress pulse in the TT has the same order of magnitude as the incident pulse and can be used to measure the displacement of the IB-S/IB-TT interface of the specimen.

The stresses in the bars are dispersion corrected (12), and then the time-shifted stresses are converted to strains in the bars. Equations 6–17 are used in calculating the average strain and stress in the specimen. Before presenting the stress-strain data, one needs to prove that the bar-specimen interface is planar and the specimen is under uni-axial stress. In addition, one also needs to comment on the stress equilibrium. If these three basic assumptions made in 1-D Hopkinson bar analysis hold true, then the experiment is considered as a valid experiment.

Three dimensionless nonplanar interface parameters, $\hat{u}_i - i = IB, TT, TB$, can be defined to express the deviation from the planar interface condition for the bar-specimen interfaces.

$$\hat{u}_{IB}(t) = (u_Z^C - u_Z^A) / u_Z^A, \quad (18)$$

$$\hat{u}_{TT}(t) = (u_Z^C - u_Z^B) / u_Z^B, \quad (19)$$

and

$$\hat{u}_{TB}(t) = (u_Z^E - u_Z^D) / u_Z^D, \quad (20)$$

where, the displacement components, u_Z^j , are outlined in figure 21, and $j = A, B, C, D, E$.

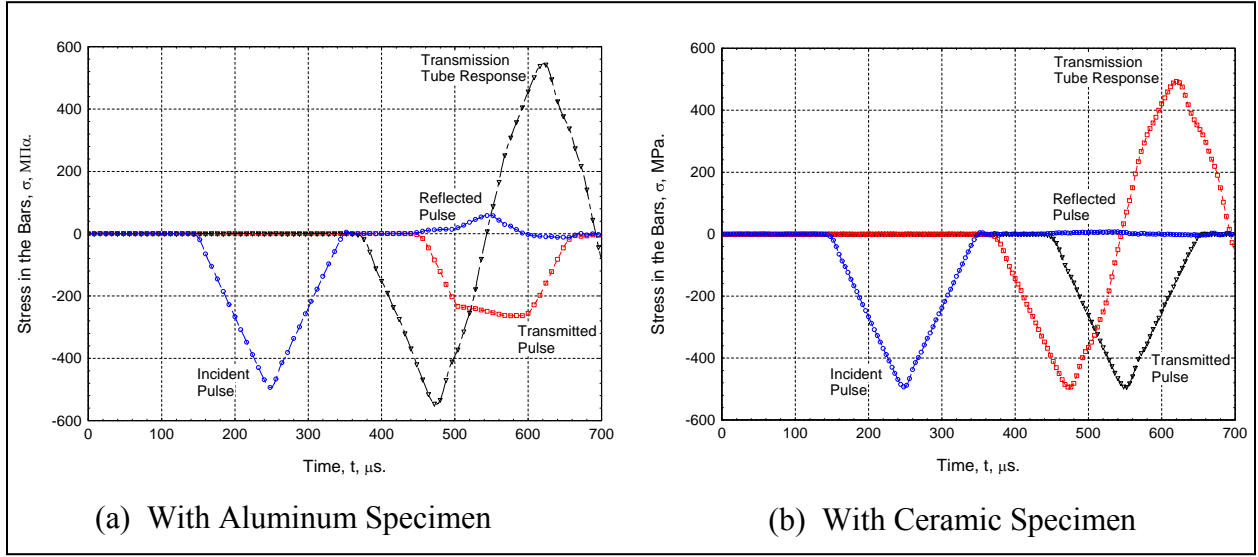


Figure 20. Bar responses of the new compression SHPB with TT.

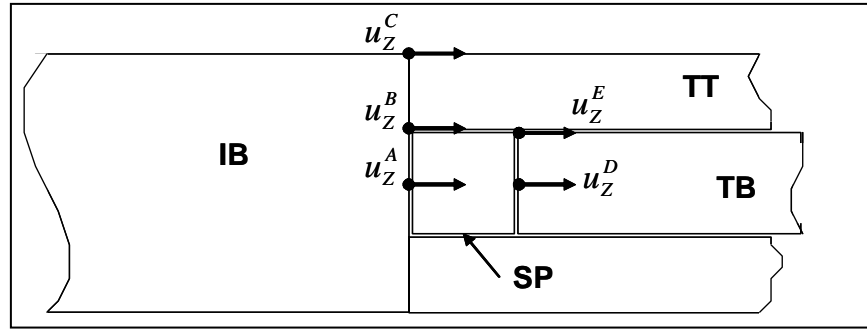


Figure 21. Notations for axial displacements measured at different radial locations of different bars.

Figures 22 and 23 show the time history of the dimensionless nonplanar interface parameters for ceramic and aluminum specimens, respectively. In these figures, the nonplanar interface parameters \hat{u}_{IB} , \hat{u}_{TT} , and \hat{u}_{TB} (given by equations 18–20) for the new compression SHPB with TT are presented and denoted by IB-S/IB-TT interface, IB-TT interface, and S-TB interface, respectively. In addition, the nonplanar interface parameters at IB-S interface and S-TB interface for classic SHPB with cylindrical specimens are also presented. The nonplanar interface parameters have maximum value at small displacements, which correspond to small time ($\hat{t} \approx 0$) and exponentially decrease to plateau level at large displacements, and can be expressed as

$$\hat{u}_i(\hat{t}) = \hat{u}_{i0} + \alpha \cdot e^{-\beta \hat{t}}, \quad (21)$$

where, \hat{u}_{i0} , α , and β are fitting constants. The fitting constant, \hat{u}_{i0} represents the plateau value and the addition of constants, $\hat{u}_{i0} + \alpha$ represent the maximum value at $\hat{t} = 0$. In the case of classic compression SHPB with cylindrical ceramic specimen (figure 21a), the parameter \hat{u}_{IB} is found to be positive with a maximum value of 0.463, which exponentially decays to a plateau value of 0.071, and the parameter \hat{u}_{TB} is found to be negative with a maximum value of -0.698 , which exponentially decays to a plateau value of -0.072 (table 3). This study proves that, in fact the bar-specimen interfaces, as described in figure 7, are nonplanar, and the curvature of the S-TB bar interface has an opposite sign to that of the IB-S interface.

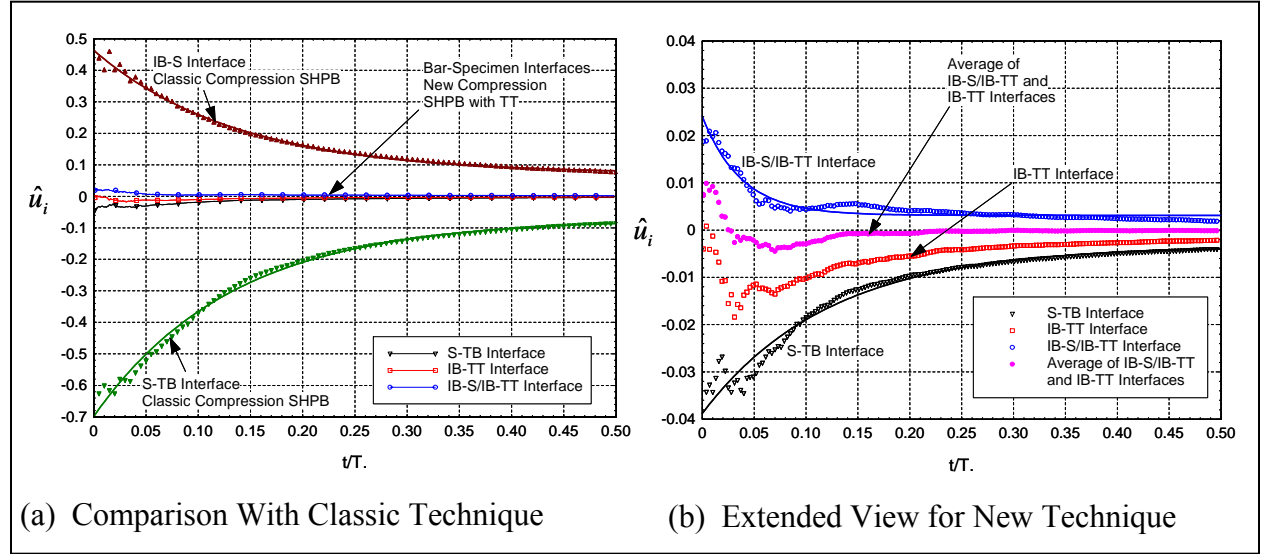


Figure 22. Nonplanar interface parameter, \hat{u}_i , as a function of time, ceramic specimen.

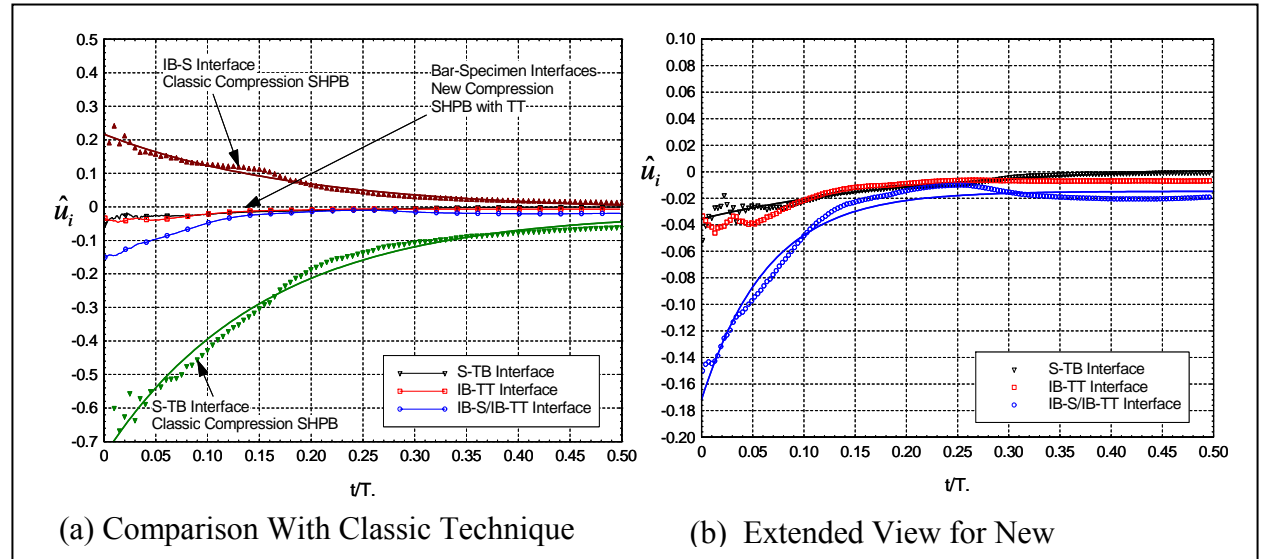


Figure 23. Nonplanar interface parameter, \hat{u}_i , as a function of time, aluminum specimen.

Table 3. Nonplanar bar-specimen interface parameters and fitting constants for ceramic specimen and steel bars.

Ceramic Specimens				
Parameters	Classic SHPB		New SHPB With TT	
	\hat{u}_{IB}	\hat{u}_{TB}	\hat{u}_{IB}	\hat{u}_{TB}
\hat{u}_{i0}	0.0709	-0.0716	0.0031	-0.0034
α	0.3920	-0.6260	0.0209	-0.0354
β	7.34	7.57	26.4	8.22

In the case of the new compression SHPB with TT and with ceramic specimen, the calculated values of the nonplanar interface parameters are an order of magnitude lower than the classic case; however, these are not absolutely zero. A little free surface on the IB-S/IB-TT interface and the specimen with different acoustic impedance than the bars are the main reasons for the finite but relatively smaller values of the nonplanar interface parameters. Figure 21b shows a close-up view of these parameters. Table 3 shows the fitting parameters of the nonplanar interface parameters for IB-S and S-TB interfaces. The plateau value at IB-S/IB-TT is found to be ($\hat{u}_{IB0} = 0.0031$), which is only 4.4% as compared to the classic case ($\hat{u}_{IB0} = 0.0709$). The maximum value in this case is found to be ($\hat{u}_{IB0} + a = 0.024$), which is $\sim 5.2\%$ of the classic value ($\hat{u}_{IB0} + a = 0.463$). Similar reduction is observed in the S-TB interface. This study validates the hypothesis made prior to the numerical experiment that the new compression SHPB with TT will guarantee a planar-bar-specimen interface condition for small-diameter-hard specimens in the elastic phase of deformation. In a realistic experimental setup, the specimen diameter should be a little less than the transmission bar, and there would be a little free surface on the IB-S/IB-TT interface, and thus the bar-specimen interfaces, will not be perfectly nonplanar. In the case of ceramic specimens and steel bars, the classic method provides 46%–70% error in small strain measurement and $\sim 7\%$ error for large strain measurements. However, this new technique with TT will provide much better accuracy than the classic method with the limit of 2%–4% error for very small strain measurement and 0.31%–0.34% error for relatively larger strains.

It is interesting to note that the error in the IB-TT interface is similar (same order of magnitude) to that of the IB-S/IB-TT interface, but is negative instead of positive. If equation 11 is used to calculate the average displacement at the IB-S/IB-TT interface, the error will be minimum (near zero) as shown in figure 22b by the legend “Average of the IB-S/IB-TT and IB-TT Interfaces.” It has been shown that the error in the S-TB interface is an order of magnitude smaller in the case of the SHPB with TT; the use of equation 14 will provide a sufficiently accurate measurement of strain in the elastic deformation phase (small strain) of a ceramic (linear-elastic) specimen.

The aluminum specimen is acoustically softer than the bars, and thus the curvature of the IB-S/IB-TT interface, in the case of SHPB with TT, is found opposite to that of the classic case (figure 23b, table 4). This implies that the particle velocity at the center of the IB

Table 4. Nonplanar bar-specimen interface parameters and fitting constants for the aluminum specimen and steel bars.

Aluminum Specimens				
Parameters	Classic SHPB		New SHPB With TT	
	\hat{u}_{IB}	\hat{u}_{TB}	\hat{u}_{IB}	\hat{u}_{TB}
\hat{u}_{i0}	-0.0114	-0.0164	-0.0147	0.0050
α	0.2280	-0.7250	-0.1570	-0.0404
β	5.27	6.52	15.6	4.55

(in contact with the specimen) is higher than the edge of the IB. In other words, the curvature of the IB-S interface has the same shape and sign as that of the S-TB interface. In this case, the displacement measured at the IB-S/IB-TT interface will be smaller than the average displacement of the specimen, and consecutively the strain measured using equation 8 will be smaller than the specimen strain. This error in displacement measurement (under prediction) at the IB-S/IB-TT interface has the same order of magnitude as compared to the classic case (over prediction); however, the amplitude error is a little smaller. On the other hand, the error in the S-TB interface is greatly improved by the new SHPB with TT method.

The amplitude of the stress pulse in the TT has the same order of magnitude as that of the incident pulse. A close examination of figure 22b and 23b reveals that the error in the IB-TT interface is negative and an order of magnitude smaller as compared to the classic case. Thus, the stress pulse of TT alone can be used to measure the displacement (equation 9) of the IB-S/IB-TT interface, irrespective of the type of the specimen. In this case, the IB responses (incident and reflected pulses) are redundant, which suggests that the length of the IB can be arbitrary. If the length of the IB is considered zero, then the compression SHPB with TT reduces to a direct impact Hopkinson pressure bar (HPB) with TT (figure 24a). One of the problems of direct impact HPB is that the displacement of the impact face of the specimen cannot be measured without a high-speed camera. If a direct impact HPB with TT is used, the displacement of the impact end of the specimen can be measured from the TT response (equation 9), and as usual, the displacement of the S-TB interface can be estimated from the TB response (equation 13).

The analysis and numerical results presented can be applied to a hollow cylindrical specimen with some changes. Figure 24b shows the application of a hollow cylindrical specimen in conjunction with an SHPB with TT and with a direct impact HPB with TT. Materials with low Poisson's ratio, e.g., metal foams, can be used as hollow cylindrical specimens. Additional cylindrical enclosures may be used to characterize materials under confinement. The new compression SHPB with TT (figure 18) and the new direct impact HPB with TT (figure 24a) guarantee the planar bar-specimen interface condition within reasonable engineering accuracy (<5%). In addition, the direct impact HPB with TT eliminates the age-old problem of

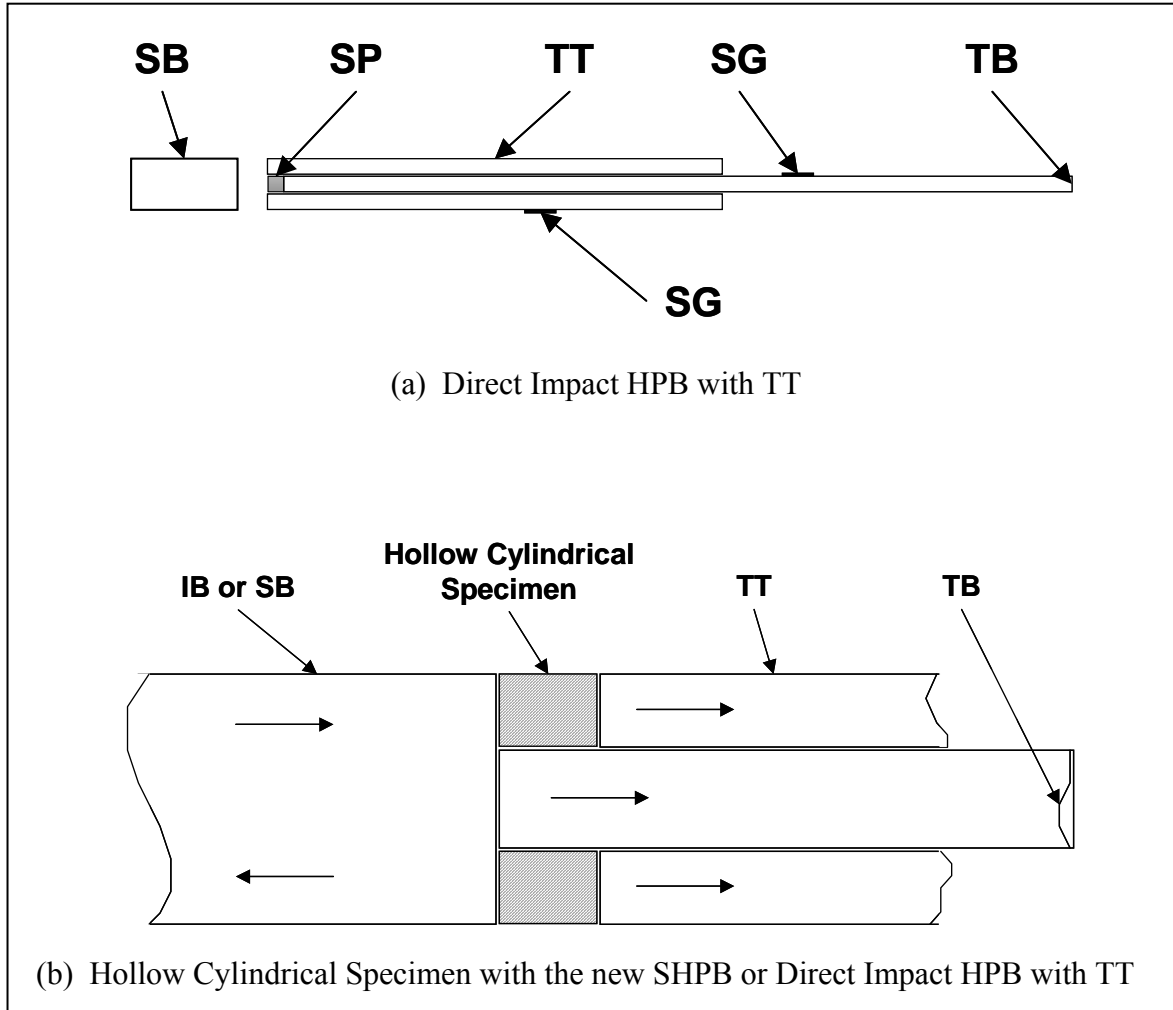


Figure 24. HPB with TT: applications with direct impact and hollow cylindrical specimen.

displacement measurement at the impact end of the specimen. Because the cylindrical specimen with chamfered edges provides uni-axial stress distribution along the length of the specimen under elastic deformation phase, the use of a cylindrical specimen with chamfered edges in conjunction with the new SHPB with TT satisfies the planar bar-specimen interface condition at all time. However, the problem of stress equilibrium in the specimen remains (figure 17). The accurate construction of a stress-strain diagram in the linear-elastic deformation phase should accurately predict the average stress in the specimen in addition to the accurate prediction of small strain/elastic deformation. The stress equilibrium in the specimen is usually not achieved (24, 27, 37) in the initial phase of elastic deformation (figure 17). It is a usual practice to use specimens with $H_s / D_s \sim 1.00$ in most SHPB applications; however, thinner specimens can provide better stress equilibrium. If thinner specimens are used, $0.01 < H_s / D_s < 0.10$, the uni-axial stress condition of the specimen changes to plane-strain condition, and in this case, friction and radial inertia effects become important. The new SHPB with TT is designed for small strain measurement in the linear-elastic deformation phase, and it can be assumed that the

friction and radial inertia effects are negligible. With this assumption, the effect of specimen thickness on the nonequilibrium stress parameter, R , is determined for three different ceramic specimens with chamfered edges, $H_S / D_S = 1.00, 0.50, 0.25$, and is presented in figure 25.

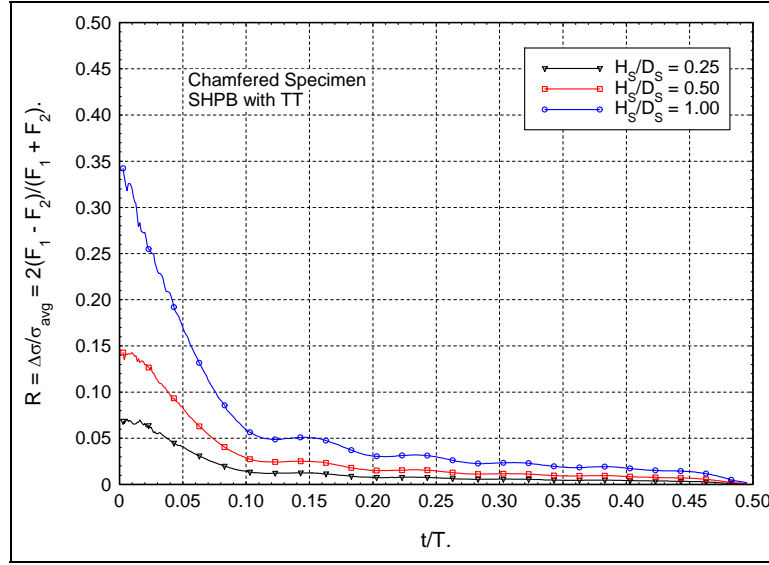


Figure 25. Deviation from the stress equilibrium of the ceramic specimen with a different H_S / D_S ratio, SHPB with TT.

Figure 25 shows that the decrease in the specimen H_S / D_S ratio decreases the nonequilibrium stress parameter, R ; however, nonequilibrium exists (37). Thus, one can plot the time-averaged nonequilibrium stress and strain data to represent engineering stress-strain relationships of the material at high strain rate (figure 26). The numerical bar responses are corrected for dispersion following the methodology proposed by Lifshitz and Leber (10). In addition, the dispersion correction algorithm for cylindrical tubes and rods proposed by Ren et al. (41) using the M-H shell model (42, 43) is also used.

The linear-elastic moduli of ceramic and aluminum used in the simulations were 370 GPa and 69 GPa, respectively. In the case of ceramic specimen (figure 26a), the moduli obtained from the simulation in the cases of classic 1-wave, 3-wave, and SHPB with TT analyses are 158, 208, and 502 GPa, respectively, which corresponds to the ratio of theoretical modulus vs. simulated modulus, $E_{\text{Theo}} / E_{\text{Simu}}$ 0.427, 0.562, and 1.357, respectively. The ratios $E_{\text{Theo}} / E_{\text{Simu}}$ for the aluminum specimen (figure 26b) in the previously mentioned cases are 0.790, 0.764, and 1.635, respectively. Clearly, the classic 1- and 3-wave analyses predict higher strains due to the nonplanar interface condition and thus lower linear-elastic modulus. The new SHPB with TT overpredicts the modulus, which proves the validity of the assumption that the bar-specimen interfaces are nonplanar. The impedance mismatch between the SP and IB, and IB and TT (note that we used steel TT) is identified as the source of this error. If the impedance of the TT is matched with that of the specimen, this error might reduce significantly, and these issues will be addressed elsewhere.

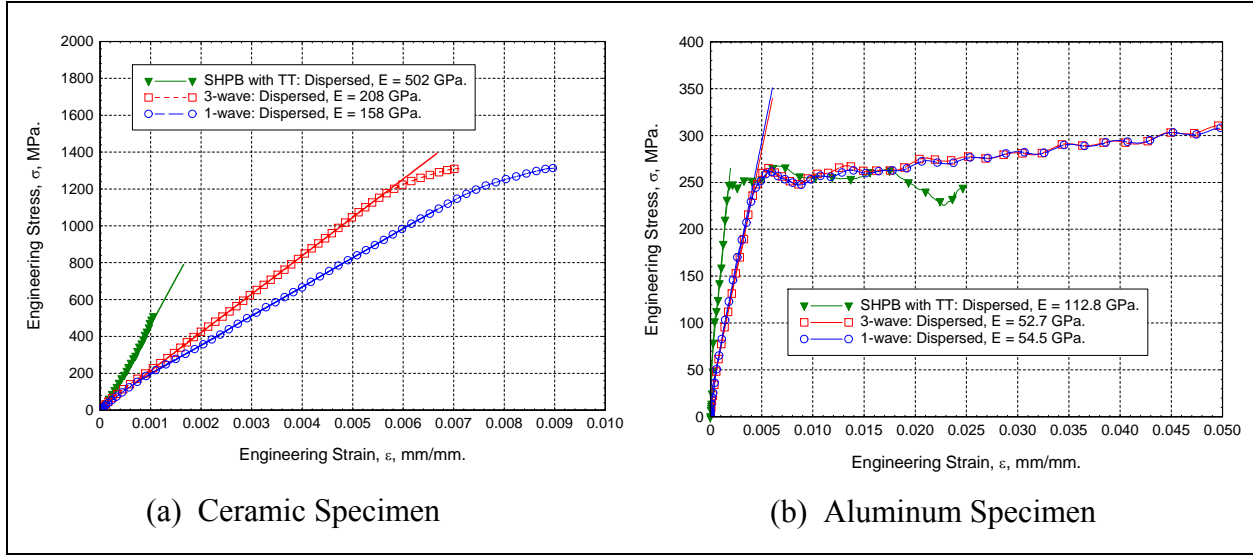


Figure 26. Stress-strain response of SHPB with TT and comparison with classic methods, H_S / D_S , $D_S / D_{IB} = 0.60$.

Zhao and Gary (44) and Zhao (45) proposed a combined analytical-numerical-experimental approach for the small strain measurement using the SHPB technique, which is computationally extensive and requires parametric evaluation of several parameters of a rate-sensitive material model, however, is considered the state-of-the-art solution of the problem. The new SHPB with TT and with the chamfered cylindrical specimen provides an experimental way of measuring small linear-elastic deformation, while satisfying all the major assumptions made in the 1-D SHPB analysis.

6. Summary

Extensive numerical analyses are carried out in the design of Hopkinson bar specimens and in new experiments that satisfy the uni-axial stress condition in the specimen and the planar bar-specimen conditions. It has been shown that a right cylindrical specimen with a chamfered specimen with a diameter smaller than the bars improves the uni-axial stress condition in the specimen. The new SHPB with TT and direct impact HPB with TT experimental techniques provide the planar bar-specimen interface condition much better than the traditional method. These new experimental techniques provide a way for small-strain measurement with sufficient engineering accuracy. The new direct impact HPB with TT solves the age-old problem of the displacement measurement at the impact end of the specimen. One-dimensional Hopkinson bar analysis is modified for the analysis of the new SHPB with TT technique. The new data analysis together with dispersion correction methodology is applied to reduce the numerical bar responses in to stress-strain diagrams. Results show that the new SHPB with TT provides better planar bar-specimen interface conditions, however, overpredicts the linear-elastic modulus, which can further be modified though the selection of impedance-matched TT.

7. References

1. Hopkinson, B. A Method of Measuring the Pressure Produced in the Detonation of High Explosives or by the Impact of Bullets. *Philosophical Transactions of the Royal Society of London, Series A, Containing Papers of a Mathematical or Physical Character* **1914**, 213, 437–456.
2. Kolsky, H. An Investigation of the Mechanical Properties of Materials at Very High Rates of Loading. *Proc. Phys. Soc., London, II-B* **1949**, 62, 676–700.
3. Davies, R. M. A Critical Study of the Hopkinson Pressure Bar. *Philosophical Transactions of the Royal Society of London, Series A, Mathematical and Physical Sciences* **1948**, 240 (821), 375–457.
4. Mechanical Testing and Evaluation, *ASM Handbook, Volume 8*; AMS International: Materials Park, OH, 2000.
5. Meyers, M. A. *Dynamic Behavior of Materials*; John Wiley & Sons: New York, 1994.
6. Daniel, I. M.; LaBedz, R. H.; Liber, T. New Methods for Testing Composites at Very High Strain Rates. *Experimental Mechanics* **1981**, 21 (2), 71–77.
7. Nemat-Nasser, S.; Issacs, J. B.; Starrett, J. E. Hopkinson Techniques for Dynamic Recovery Experiments. *Proceedings of the Royal Society of London, Series A* **1991**, 453, 371–391.
8. Nemat-Nasser, S.; Isaacs, J.; Rome J. Triaxial Hopkinson Techniques, Mechanical Testing and Evaluation, *ASM Handbook, Volume 8*; ASM International: Materials Park, OH, 2000; pp 516–518.
9. Chen, W.; Zhang, B.; Forrestal, M. J. A Split Hopkinson Bar Technique for Low Impedance Materials. *Experimental Mechanics* **1999**, 39, 1–5.
10. Lifshitz, J. M.; Leber, H. Data Processing in the Split Hopkinson Pressure Bar Tests *International Journal of Impact Engineering* **1994**, 15 (6), 723–733.
11. Bussac, M. N.; Collet, P.; Gary, G.; Othman, R. An Optimization Method for Separating and Rebuilding One-Dimensional Dispersive Waves From Multi-Point Measurements: Application to Elastic or Viscoelastic Bars. *Journal of the Mechanics and Physics of Solids* **2002**, 50, 321–349.
12. Gama, B. A.; Lopatnikov, S. L.; Gillespie, J. W., Jr. Hopkinson Bar Experimental Technique: A Critical Review. *Applied Mechanics Review* **August 2003**.

13. Gama, B. A.; Lopatnikov, S. L.; Gillespie, J. W., Jr. Numerical Hopkinson Bar Analysis: Validity of One-Dimensional Assumptions. *ASC 2003 Conference*, Gainesville, FL, 20–22 October 2003.
14. Lindholm, U. S.; Yeakley, L. M. High Strain Rate Testing: Tension and Compression. *Experimental Mechanics* **1968**, *8*, 1–9.
15. Nicholas, T. Tensile Testing of Materials at High Rates of Strain. *Experimental Mechanics* **1980**, *21*, 177–185.
16. Noble, J. P.; Goldthorpe, B. D.; Church, P.; Harding, J. The Use of the Hopkinson Bar to Validate Constitutive Relations at High Rates of Strain. *Journal of Mechanics and Physics of Solids* **1999**, *47*, 1187–1206.
17. Rodriguez, J.; Chocron, I. S.; Martinez, M. A.; Sanchez Galvez, V. High Strain Rate Properties of Aramid and Polyethylene Woven Fabric Composites. *Composites, Part B*, **1996**, *27B*, 147–154.
18. Chocron Benloulou, I. S.; Rodriguez, J.; Martinez, M. A.; Sanchez Galvez, V. Dynamic Tensile Testing of Aramid and Polyethylene Fiber Composites. *International Journal of Impact Engineering* **1997**, *19* (2), 135–146.
19. Melin, L. G.; Asp, L. E. Effects of Strain Rate on Transverse Tension Properties of a Carbon/Epoxy Composite: Studied by Moire Photography. *Composites, Part A*, **1999**, *30*, 305–316.
20. Eskandari, H.; Nemes, J. A. Dynamic Testing of Composite Laminates With a Tensile Split Hopkinson Bar. *Journal of Composite Materials* **2000**, *33* (4), 260–273.
21. Harding, J.; Huddart, J. The Use of the Double-Notch Shear Test in Determining the Mechanical Properties of Uranium at Very High Rates of Strain. *Proceedings of the 2nd International Conference on Mechanical Properties at High Rates of Strain*; Harding, J., Ed., The Institute of Physics: London, 1980, vol. 47, pp 49–61.
22. Ferguson, W. G.; Hauser, J. E.; Dorn, J. E. The Dynamic Punching of Metals, Dislocation Damping in Zinc Single Crystals. *Britt. J. Appl. Phys.* **1967**, *18*, 411–417.
23. Gilat, A. Torsional Kolsky Bar Testing, Mechanical Testing and Evaluation, *ASM Handbook, Volume 8*, ASM International: Materials Park, OH, 2000; pp 505–515.
24. Gray, G. T., III. Classic Split-Hopkinson Pressure Bar Testing, Mechanical Testing and Evaluation, *ASM Handbook, Volume 8*; ASM International: Materials Park, OH, 2000; pp 462–476.
25. Davies, E. D. H.; Hunter, S. C. The Dynamic Compression Testing of Solids by the Method of Split Hopkinson Pressure Bar (SHPB). *J. Mech. Phys. Solids* **1963**, *11*, 155–179.

26. Follansbee, P. S. The Hopkinson Bar, Mechanical Testing and Evaluation, *ASM Handbook, Volume 8*; ASM International: Materials Park, OH, 1995; pp 198–203.
27. Subhash, G.; Ravichandran, G. Split-Hopkinson Pressure Bar Testing of Ceramics, Mechanical Testing and Evaluation, *ASM Handbook, Volume 8*; ASM International: Materials Park, OH, 2000; pp 488–496.
28. Malinowski, J. Z.; Klepaczko, J. R. Unified Analytic and Numerical Approach to Specimen Behavior in the Split Hopkinson Pressure Bar. *International Journal of Mechanical Sciences* **1986**, 28 (6), 381–391.
29. Gray, G. T., III. Split-Hopkinson Pressure Bar Testing of Soft Materials, Mechanical Testing and Evaluation, *ASM Handbook, Volume 8*; ASM International: Materials Park, OH, 2000; pp 488–496.
30. Chen, W.; Zhang, B.; Forrestal, M. J. A Split Hopkinson Bar Technique for Low Impedance Materials. *Experimental Mechanics* **1999**, 39, 1–5.
31. Harding, J. Effect of Strain Rate and Specimen Geometry on the Compressive Strength of Woven Glass-Reinforced Epoxy Laminates. *Composites* **1993**, 24 (4), 323–332.
32. Takeda, N.; Wan, L. Impact Compression Damage Evolution in Unidirectional Glass Fiber Reinforced Polymer Composites, ASME, *AD in High Strain Rate Effects on Polymer, Metal and Ceramic Matrix Composites and Other Advanced Materials* **1995**, 48, 109–113.
33. Leber, H.; Lifshitz, J. M. Interlaminar Shear Behavior of Plain-Weave GRP at Static and High Rates of Strain. *Composites Science and Technology* **1996**, 56 (4), 391–405.
34. Deltort, B.; Neme, A.; Tanguy, B. New Specimen Geometry for Compression Hopkinson Bars. *Journal De Physique, IV* **1997**, 7 (3), C3-265–C3-270.
35. Ninan, L.; Tsai, J.; Sun, C. T. Use of Split Hopkinson Pressure Bar for Testing Off-Axis Composites. *International Journal of Impact Engineering* **2001**, 25, 291–313.
36. Bertholf, L. D.; Karnes, C. H. Two-Dimensional Analysis of the Split Hopkinson Pressure Bar System. *Journal of Mechanics and Physics of Solids* **1975**, 23, 1–19.
37. Zencker, U.; Clos, R. Limiting Conditions for Compression Testing of Flat Specimens in the Split Hopkinson Pressure Bar. *Experimental Mechanics* **1999**, 39 (4), 343–348.
38. Anderson C. E., Jr.; O'Donoghue, P. E.; Lankford, J.; Walker, J. D. Numerical Simulation of SHPB Experiments for the Dynamic Compressive Strength and Failure of Ceramics. *International Journal of Fracture* **1992**, 55, 193–208.

39. Lopatnikov, S. L.; Gama, B. A.; Krauthauser, C.; Gillespie, J. W., Jr. On the Classic Split-Hopkinson Pressure Bar (SHPB) Analysis. *Technical Physics Letters* **2004**, *30* (2), 39–46.
40. Pochhammer, L. Über Fortpflanzungsgeschwindigkeiten kleiner Schwindungen in einem unbegrenzten isotropen Kreiszylinder. *Journal reine angewandte Mathematik (Creele)* **1876**, *81*, 324.
41. Ren, L.; Larson, M.; Gama, B. A.; Gillespie, J. W., Jr. Wave Dispersion in Cylindrical Tubes: Applications to Hopkinson Pressure Bar Experimental Techniques. *International Journal of Impact Engineering*, submitted for publication, May 2003.
42. Herrmann, G.; Mirsky, I. Three-Dimensional and Shell-Theory Analysis of Axially Symmetric Motions of Cylinders. *Journal of Applied Mechanics* **1956**, *23*, 563–568.
43. Mirsky, I.; Herrmann, G. Axially Symmetric Motions of Thick Cylindrical Shells. *Journal of Applied Mechanics* **1958**, *25*, 97–102.
44. Zhao, H.; Gary, G. On the Use of SHPB Techniques to Determine the Dynamic Behavior of Materials in the Range of Small Strains. *International Journal of Solids and Structures* **1996**, *33* (23), 3363–3375.
45. Zhao, H. A Study on Testing Techniques for Concrete-Like Materials Under Compressive Impact Loading. *Cement and Concrete Composites* **1998**, *20*, 293–299.

NO. OF
COPIES ORGANIZATION

1 DEFENSE TECHNICAL
(PDF INFORMATION CTR
ONLY) DTIC OCA
8725 JOHN J KINGMAN RD
STE 0944
FT BELVOIR VA 22060-6218

1 COMMANDING GENERAL
US ARMY MATERIEL CMD
AMCRDA TF
5001 EISENHOWER AVE
ALEXANDRIA VA 22333-0001

1 INST FOR ADVNCD TCHNLGY
THE UNIV OF TEXAS
AT AUSTIN
3925 W BRAKER LN STE 400
AUSTIN TX 78759-5316

1 US MILITARY ACADEMY
MATH SCI CTR EXCELLENCE
MADN MATH
THAYER HALL
WEST POINT NY 10996-1786

1 DIRECTOR
US ARMY RESEARCH LAB
IMNE AD IM DR
2800 POWDER MILL RD
ADELPHI MD 20783-1197

3 DIRECTOR
US ARMY RESEARCH LAB
AMSRD ARL CI OK TL
2800 POWDER MILL RD
ADELPHI MD 20783-1197

3 DIRECTOR
US ARMY RESEARCH LAB
AMSRD ARL CS IS T
2800 POWDER MILL RD
ADELPHI MD 20783-1197

NO. OF
COPIES ORGANIZATION

ABERDEEN PROVING GROUND

1 DIR USARL
AMSRD ARL CI OK TP (BLDG 4600)

NO. OF
COPIES ORGANIZATION

1 DIRECTOR
US ARMY RESEARCH LAB
AMSRD ARL SE L
D SNIDER
2800 POWDER MILL RD
ADELPHI MD 20783-1197

1 DIRECTOR
US ARMY RESEARCH LAB
AMSRD ARL SE DE
R ATKINSON
2800 POWDER MILL RD
ADELPHI MD 20783-1197

5 DIRECTOR
US ARMY RESEARCH LAB
AMSRD ARL WM MB
A ABRAHAMIAN
M BERMAN
M CHOWDHURY
T LI
E SZYMANSKI
2800 POWDER MILL RD
ADELPHI MD 20783-1197

1 COMMANDER
US ARMY MATERIEL CMD
AMXMI INT
5001 EISENHOWER AVE
ALEXANDRIA VA 22333-0001

2 PM MAS
SFAE AMO MAS MC
PICATINNY ARSENAL NJ
07806-5000

3 COMMANDER
US ARMY ARDEC
AMSTA AR CC
M PADGETT
J HEDDERICH
H OPAT
PICATINNY ARSENAL NJ
07806-5000

2 COMMANDER
US ARMY ARDEC
AMSTA AR AE WW
E BAKER
J PEARSON
PICATINNY ARSENAL NJ
07806-5000

NO. OF
COPIES ORGANIZATION

1 COMMANDER
US ARMY ARDEC
AMSTA AR FSE
PICATINNY ARSENAL NJ
07806-5000

1 COMMANDER
US ARMY ARDEC
AMSTA AR TD
PICATINNY ARSENAL NJ
07806-5000

13 COMMANDER
US ARMY ARDEC
AMSTA AR CCH A
F ALTAMURA
M NICOLICH
M PALATHINGUL
D VO
R HOWELL
A VELLA
M YOUNG
L MANOLE
S MUSALLI
R CARR
M LUCIANO
E LOGSDEN
T LOUZEIRO
PICATINNY ARSENAL NJ
07806-5000

1 COMMANDER
US ARMY ARDEC
AMSTA AR CCH P
J LUTZ
PICATINNY ARSENAL NJ
07806-5000

1 COMMANDER
US ARMY ARDEC
AMSTA AR FSF T
C LIVECCHIA
PICATINNY ARSENAL NJ
07806-5000

1 COMMANDER
US ARMY ARDEC
AMSTA ASF
PICATINNY ARSENAL NJ
07806-5000

<u>NO. OF COPIES</u>	<u>ORGANIZATION</u>
1	COMMANDER US ARMY ARDEC AMSTA AR QAC T C J PAGE PICATINNY ARSENAL NJ 07806-5000
1	COMMANDER US ARMY ARDEC AMSTA AR M D DEMELLA PICATINNY ARSENAL NJ 07806-5000
3	COMMANDER US ARMY ARDEC AMSTA AR FSA A WARNASH B MACHAK M CHIEFA PICATINNY ARSENAL NJ 07806-5000
2	COMMANDER US ARMY ARDEC AMSTA AR FSP G M SCHIKSNIS D CARLUCCI PICATINNY ARSENAL NJ 07806-5000
2	COMMANDER US ARMY ARDEC AMSTA AR CCH C H CHANIN S CHICO PICATINNY ARSENAL NJ 07806-5000
1	COMMANDER US ARMY ARDEC AMSTA AR QAC T D RIGOGLIOSO PICATINNY ARSENAL NJ 07806-5000
1	COMMANDER US ARMY ARDEC AMSTA AR WET T SACHAR BLDG 172 PICATINNY ARSENAL NJ 07806-5000

<u>NO. OF COPIES</u>	<u>ORGANIZATION</u>
1	US ARMY ARDEC INTELLIGENCE SPECIALIST AMSTA AR WEL F M GUERRIERE PICATINNY ARSENAL NJ 07806-5000
10	COMMANDER US ARMY ARDEC AMSTA AR CCH B P DONADIA F DONLON P VALENTI C KNUTSON G EUSTICE K HENRY J MCNABOC G WAGNECZ R SAYER F CHANG PICATINNY ARSENAL NJ 07806-5000
6	COMMANDER US ARMY ARDEC AMSTA AR CCL F PUZYCKI R MCHUGH D CONWAY E JAROSZEWSKI R SCHLENNER M CLUNE PICATINNY ARSENAL NJ 07806-5000
1	PM ARMS SFAE GCSS ARMS BLDG 171 PICATINNY ARSENAL NJ 07806-5000
1	COMMANDER US ARMY ARDEC AMSTA AR WEA J BRESCIA PICATINNY ARSENAL NJ 07806-5000
1	PM MAS SFAE AMO MAS PICATINNY ARSENAL NJ 07806-5000

NO. OF
COPIES ORGANIZATION

1 PM MAS
SFAE AMO MAS
CHIEF ENGINEER
PICATINNY ARSENAL NJ
07806-5000

1 PM MAS
SFAE AMO MAS PS
PICATINNY ARSENAL NJ
07806-5000

2 PM MAS
SFAE AMO MAS LC
PICATINNY ARSENAL NJ
07806-5000

1 COMMANDER
US ARMY ARDEC
PRODUCTION BASE
MODERN ACTY
AMSMC PBM K
PICATINNY ARSENAL NJ
07806-5000

1 COMMANDER
US ARMY TACOM
PM COMBAT SYSTEMS
SFAE GCS CS
6501 ELEVEN MILE RD
WARREN MI 48397-5000

1 COMMANDER
US ARMY TACOM
AMSTA SF
WARREN MI 48397-5000

1 DIRECTOR
AIR FORCE RESEARCH LAB
MLLMD
D MIRACLE
2230 TENTH ST
WRIGHT PATTERSON AFB OH
45433-7817

1 OFC OF NAVAL RESEARCH
J CHRISTODOULOU
ONR CODE 332
800 N QUINCY ST
ARLINGTON VA 22217-5600

1 US ARMY CERL
R LAMPO
2902 NEWMARK DR
CHAMPAIGN IL 61822

NO. OF
COPIES ORGANIZATION

1 COMMANDER
US ARMY TACOM
PM SURVIVABLE SYSTEMS
SFAE GCSS W GSI H
M RYZYI
6501 ELEVEN MILE RD
WARREN MI 48397-5000

1 COMMANDER
US ARMY TACOM
CHIEF ABRAMS TESTING
SFAE GCSS W AB QT
T KRASKIEWICZ
6501 ELEVEN MILE RD
WARREN MI 48397-5000

1 COMMANDER
WATERVLIET ARSENAL
SMCWV QAE Q
B VANINA
BLDG 44
WATERVLIET NY 12189-4050

1 TNG, DOC, & CBT DEV
ATZK TDD IRSA
A POMEY
FT KNOX KY 40121

2 HQ IOC TANK
AMMUNITION TEAM
AMSIO SMT
R CRAWFORD
W HARRIS
ROCK ISLAND IL 61299-6000

2 COMMANDER
US ARMY AMCOM
AVIATION APPLIED TECH DIR
J SCHUCK
FT EUSTIS VA 23604-5577

1 NSWC
DAHLGREN DIV CODE G06
DAHLGREN VA 22448

2 US ARMY CORPS OF ENGR
CERD C
T LIU
CEW ET
T TAN
20 MASSACHUSETTS AVE NW
WASHINGTON DC 20314

NO. OF
COPIES ORGANIZATION

1 US ARMY COLD REGIONS
RSCH & ENGRNG LAB
P DUTTA
72 LYME RD
HANOVER NH 03755

14 COMMANDER
US ARMY TACOM
AMSTA TR R
R MCCLELLAND
D THOMAS
J BENNETT
D HANSEN
AMSTA JSK
S GOODMAN
J FLORENCE
K IYER
D TEMPLETON
A SCHUMACHER
AMSTA TR D
D OSTBERG
L HINOJOSA
B RAJU
AMSTA CS SF
H HUTCHINSON
F SCHWARZ
WARREN MI 48397-5000

14 BENET LABS
AMSTA AR CCB
R FISCELLA
M SOJA
E KATHE
M SCAVULO
G SPENCER
P WHEELER
S KRUPSKI
J VASILAKIS
G FRIAR
R HASENBEIN
AMSTA CCB R
S SOPOK
E HYLAND
D CRAYON
R DILLON
WATERVLIET NY 12189-4050

1 USA SBCCOM PM SOLDIER SPT
AMSSB PM RSS A
J CONNORS
KANSAS ST
NATICK MA 01760-5057

NO. OF
COPIES ORGANIZATION

1 NSW
TECH LIBRARY CODE 323
17320 DAHLGREN RD
DAHLGREN VA 22448

2 USA SBCCOM
MATERIAL SCIENCE TEAM
AMSSB RSS
J HERBERT
M SENNETT
KANSAS ST
NATICK MA 01760-5057

2 OFC OF NAVAL RESEARCH
D SIEGEL CODE 351
J KELLY
800 N QUINCY ST
ARLINGTON VA 22217-5660

1 NSW
CRANE DIVISION
M JOHNSON CODE 20H4
LOUISVILLE KY 40214-5245

2 NSW
U SORATHIA
C WILLIAMS CD 6551
9500 MACARTHUR BLVD
WEST BETHESDA MD 20817

2 COMMANDER
NSWC
CARDEROCK DIVISION
R PETERSON CODE 2020
M CRITCHFIELD CODE 1730
BETHESDA MD 20084

8 DIRECTOR
US ARMY NGIC
D LEITER MS 404
M HOLTUS MS 301
M WOLFE MS 307
S MINGLEDORF MS 504
J GASTON MS 301
W GSTATTENBAUER MS 304
R WARNER MS 305
J CRIDER MS 306
2055 BOULDERS RD
CHARLOTTESVILLE VA
22911-8318

NO. OF
COPIES ORGANIZATION

1 NAVAL SEA SYSTEMS CMD
D LIESE
1333 ISAAC HULL AVE SE 1100
WASHINGTON DC 20376-1100

1 EXPEDITIONARY WARFARE
DIV N85
F SHOUP
2000 NAVY PENTAGON
WASHINGTON DC 20350-2000

8 US ARMY SBCCOM
SOLDIER SYSTEMS CENTER
BALLISTICS TEAM
J WARD
W ZUKAS
P CUNNIFF
J SONG
MARINE CORPS TEAM
J MACKIEWICZ
BUS AREA ADVOCACY TEAM
W HASKELL
AMSSB RCP SS
W NYKVIST
S BEAUDOIN
KANSAS ST
NATICK MA 01760-5019

7 US ARMY RESEARCH OFC
A CROWSON
H EVERETT
J PRATER
G ANDERSON
D STEPP
D KISEROW
J CHANG
PO BOX 12211
RESEARCH TRIANGLE PARK NC
27709-2211

1 AFRL MLBC
2941 P ST RM 136
WRIGHT PATTERSON AFB OH
45433-7750

1 DIRECTOR
LOS ALAMOS NATL LAB
F L ADDESSIO T 3 MS 5000
PO BOX 1633
LOS ALAMOS NM 87545

NO. OF
COPIES ORGANIZATION

8 NSW
J FRANCIS CODE G30
D WILSON CODE G32
R D COOPER CODE G32
J FRAYSSE CODE G33
E ROWE CODE G33
T DURAN CODE G33
L DE SIMONE CODE G33
R HUBBARD CODE G33
DAHLGREN VA 22448

1 NSW
CARDEROCK DIVISION
R CRANE CODE 6553
9500 MACARTHUR BLVD
WEST BETHESDA MD 20817-5700

1 AFRL MLSS
R THOMSON
2179 12TH ST RM 122
WRIGHT PATTERSON AFB OH
45433-7718

2 AFRL
F ABRAMS
J BROWN
BLDG 653
2977 P ST STE 6
WRIGHT PATTERSON AFB OH
45433-7739

5 DIRECTOR
LLNL
R CHRISTENSEN
S DETERESA
F MAGNESS
M FINGER MS 313
M MURPHY L 282
PO BOX 808
LIVERMORE CA 94550

1 AFRL MLS OL
L COULTER
5851 F AVE
BLDG 849 RM AD1A
HILL AFB UT 84056-5713

1 OSD
JOINT CCD TEST FORCE
OSD JCCD
R WILLIAMS
3909 HALLS FERRY RD
VICKSBURG MS 29180-6199

NO. OF
COPIES ORGANIZATION

3 DARPA
M VANFOSSSEN
S WAX
L CHRISTODOULOU
3701 N FAIRFAX DR
ARLINGTON VA 22203-1714

2 SERDP PROGRAM OFC
PM P2
C PELLERIN
B SMITH
901 N STUART ST STE 303
ARLINGTON VA 22203

1 OAK RIDGE NATL LAB
R M DAVIS
PO BOX 2008
OAK RIDGE TN 37831-6195

1 OAK RIDGE NATL LAB
C EBERLE MS 8048
PO BOX 2008
OAK RIDGE TN 37831

3 DIRECTOR
SANDIA NATL LABS
APPLIED MECHS DEPT
MS 9042
J HANDROCK
Y R KAN
J LAUFFER
PO BOX 969
LIVERMORE CA 94551-0969

1 OAK RIDGE NATL LAB
C D WARREN MS 8039
PO BOX 2008
OAK RIDGE TN 37831

4 NIST
M VANLANDINGHAM MS 8621
J CHIN MS 8621
J MARTIN MS 8621
D DUTHINH MS 8611
100 BUREAU DR
GAITHERSBURG MD 20899

1 HYDROGEOLOGIC INC
SERDP ESTCP SPT OFC
S WALSH
1155 HERNDON PKWY STE 900
HERNDON VA 20170

NO. OF
COPIES ORGANIZATION

3 NASA LANGLEY RESEARCH CTR
AMSRD ARL VS
W ELBER MS 266
F BARTLETT JR MS 266
G FARLEY MS 266
HAMPTON VA 23681-0001

1 NASA LANGLEY RESEARCH CTR
T GATES MS 188E
HAMPTON VA 23661-3400

1 FHWA
E MUNLEY
6300 GEORGETOWN PIKE
MCLEAN VA 22101

1 USDOT FEDERAL RAILROAD
M FATEH RDV 31
WASHINGTON DC 20590

3 CYTEC FIBERITE
R DUNNE
D KOHLI
R MAYHEW
1300 REVOLUTION ST
HAVRE DE GRACE MD 21078

1 DIRECTOR
NGIC
IANG TMT
2055 BOULDERS RD
CHARLOTTESVILLE VA
22911-8318

1 SIOUX MFG
B KRIEL
PO BOX 400
FT TOTTEN ND 58335

2 3TEX CORP
A BOGDANOVICH
J SINGLETARY
109 MACKENAN DR
CARY NC 27511

1 3M CORP
J SKILDUM
3M CENTER BLDG 60 IN 01
ST PAUL MN 55144-1000

NO. OF
COPIES ORGANIZATION

1 DIRECTOR
DEFENSE INTLLGNC AGNCY
TA 5
K CRELLING
WASHINGTON DC 20310

1 ADVANCED GLASS FIBER YARNS
T COLLINS
281 SPRING RUN LANE STE A
DOWNINGTON PA 19335

1 COMPOSITE MATERIALS INC
D SHORTT
19105 63 AVE NE
PO BOX 25
ARLINGTON WA 98223

1 JPS GLASS
L CARTER
PO BOX 260
SLATER RD
SLATER SC 29683

1 COMPOSITE MATERIALS INC
R HOLLAND
11 JEWEL CT
ORINDA CA 94563

1 COMPOSITE MATERIALS INC
C RILEY
14530 S ANSON AVE
SANTA FE SPRINGS CA 90670

2 SIMULA
J COLTMAN
R HUYETT
10016 S 51ST ST
PHOENIX AZ 85044

2 PROTECTION MATERIALS INC
M MILLER
F CRILLEY
14000 NW 58 CT
MIAMI LAKES FL 33014

2 FOSTER MILLER
M ROYLANCE
W ZUKAS
195 BEAR HILL RD
WALTHAM MA 02354-1196

NO. OF
COPIES ORGANIZATION

1 ROM DEVELOPMENT CORP
R O MEARA
136 SWINEBURNE ROW
BRICK MARKET PLACE
NEWPORT RI 02840

2 TEXTRON SYSTEMS
T FOLTZ
M TREASURE
1449 MIDDLESEX ST
LOWELL MA 01851

1 O GARA HESS & EISENHARDT
M GILLESPIE
9113 LESAINTE DR
FAIRFIELD OH 45014

2 MILLIKEN RESEARCH CORP
H KUHN
M MACLEOD
PO BOX 1926
SPARTANBURG SC 29303

1 CONNEAUGHT INDUSTRIES INC
J SANTOS
PO BOX 1425
COVENTRY RI 02816

1 ARMTEC DEFENSE PRODUCTS
S DYER
85 901 AVE 53
PO BOX 848
COACHELLA CA 92236

1 NATL COMPOSITE CTR
T CORDELL
2000 COMPOSITE DR
KETTERING OH 45420

3 PACIFIC NORTHWEST LAB
M SMITH
G VAN ARSDALE
R SHIPPELL
PO BOX 999
RICHLAND WA 99352

1 SAIC
M PALMER
1410 SPRING HILL RD STE 400
MS SH4 5
MCLEAN VA 22102

NO. OF
COPIES ORGANIZATION

1 ALLIANT TECHSYSTEMS INC
4700 NATHAN LN N
PLYMOUTH MN 55442-2512

1 APPLIED COMPOSITES
W GRISCH
333 NORTH SIXTH ST
ST CHARLES IL 60174

1 CUSTOM ANALYTICAL
ENG SYS INC
A ALEXANDER
13000 TENSOR LANE NE
FLINTSTONE MD 21530

1 AAI CORP
DR N B MCNELLIS
PO BOX 126
HUNT VALLEY MD 21030-0126

1 OFC DEPUTY UNDER SEC DEFNS
J THOMPSON
1745 JEFFERSON DAVIS HWY
CRYSTAL SQ 4 STE 501
ARLINGTON VA 22202

3 ALLIANT TECHSYSTEMS INC
J CONDON
E LYNAM
J GERHARD
WV01 16 STATE RT 956
PO BOX 210
ROCKET CENTER WV
26726-0210

1 PROJECTILE TECHNOLOGY INC
515 GILES ST
HAVRE DE GRACE MD 21078

1 HEXCEL INC
R BOE
PO BOX 18748
SALT LAKE CITY UT 84118

1 PRATT & WHITNEY
C WATSON
400 MAIN ST MS 114 37
EAST HARTFORD CT 06108

NO. OF
COPIES ORGANIZATION

5 NORTHROP GRUMMAN
B IRWIN
K EVANS
D EWART
A SHREKENHAMER
J MCGLYNN
BLDG 160 DEPT 3700
1100 WEST HOLLYVALE ST
AZUSA CA 91701

1 HERCULES INC
HERCULES PLAZA
WILMINGTON DE 19894

1 BRIGS COMPANY
J BACKOFEN
2668 PETERBOROUGH ST
HERNDON VA 22071-2443

1 ZERNOW TECHNICAL SERVICES
L ZERNOW
425 W BONITA AVE STE 208
SAN DIMAS CA 91773

1 GENERAL DYNAMICS OTS
L WHITMORE
10101 NINTH ST NORTH
ST PETERSBURG FL 33702

2 GENERAL DYNAMICS OTS
FLINCHBAUGH DIV
K LINDE
T LYNCH
PO BOX 127
RED LION PA 17356

1 GKN WESTLAND AEROSPACE
D OLDS
450 MURDOCK AVE
MERIDEN CT 06450-8324

2 BOEING ROTORCRAFT
P MINGURT
P HANDEL
800 B PUTNAM BLVD
WALLINGFORD PA 19086

NO. OF
COPIES ORGANIZATION

5 SIKORSKY AIRCRAFT
G JACARUSO
T CARSTENSAN
B KAY
S GARBO MS S330A
J ADELMANN
6900 MAIN ST
PO BOX 9729
STRATFORD CT 06497-9729

1 AEROSPACE CORP
G HAWKINS M4 945
2350 E EL SEGUNDO BLVD
EL SEGUNDO CA 90245

2 CYTEC FIBERITE
M LIN
W WEB
1440 N KRAEMER BLVD
ANAHEIM CA 92806

2 UDLP
G THOMAS
M MACLEAN
PO BOX 58123
SANTA CLARA CA 95052

1 UDLP WARREN OFC
A LEE
31201 CHICAGO RD SOUTH
SUITE B102
WARREN MI 48093

2 UDLP
R BRYNSVOLD
P JANKE MS 170
4800 EAST RIVER RD
MINNEAPOLIS MN 55421-1498

1 LOCKHEED MARTIN
SKUNK WORKS
D FORTNEY
1011 LOCKHEED WAY
PALMDALE CA 93599-2502

1 LOCKHEED MARTIN
R FIELDS
5537 PGA BLVD
SUITE 4516
ORLANDO FL 32839

NO. OF
COPIES ORGANIZATION

1 NORTHROP GRUMMAN CORP
ELECTRONIC SENSORS
& SYSTEMS DIV
E SCHOCH MS V 16
1745A W NURSERY RD
LINTHICUM MD 21090

1 GDLS DIVISION
D BARTLE
PO BOX 1901
WARREN MI 48090

2 GDLS
D REES
M PASIK
PO BOX 2074
WARREN MI 48090-2074

1 GDLS
MUSKEGON OPER
M SOIMAR
76 GETTY ST
MUSKEGON MI 49442

1 GENERAL DYNAMICS
AMPHIBIOUS SYS
SURVIVABILITY LEAD
G WALKER
991 ANNAPOLIS WAY
WOODBIDGE VA 22191

6 INST FOR ADVANCED
TECH
H FAIR
I MCNAB
P SULLIVAN
S BLESS
W REINECKE
C PERSAD
3925 W BRAKER LN STE 400
AUSTIN TX 78759-5316

1 ARROW TECH ASSOC
1233 SHELBURNE RD STE D8
SOUTH BURLINGTON VT
05403-7700

1 R EICHELBERGER
CONSULTANT
409 W CATHERINE ST
BEL AIR MD 21014-3613

NO. OF
COPIES ORGANIZATION

1 SAIC
G CHRYSSOMALLIS
8500 NORMANDALE LAKE BLVD
SUITE 1610
BLOOMINGTON MN 55437-3828

1 UCLA MANE DEPT ENGR IV
H T HAHN
LOS ANGELES CA 90024-1597

2 UNIV OF DAYTON
RESEARCH INST
R Y KIM
A K ROY
300 COLLEGE PARK AVE
DAYTON OH 45469-0168

1 UMASS LOWELL
PLASTICS DEPT
N SCHOTT
1 UNIVERSITY AVE
LOWELL MA 01854

1 IIT RESEARCH CTR
D ROSE
201 MILL ST
ROME NY 13440-6916

1 GA TECH RESEARCH INST
GA INST OF TCHNLGY
P FRIEDERICH
ATLANTA GA 30392

1 MICHIGAN ST UNIV
MSM DEPT
R AVERILL
3515 EB
EAST LANSING MI 48824-1226

1 UNIV OF WYOMING
D ADAMS
PO BOX 3295
LARAMIE WY 82071

1 PENN STATE UNIV
R S ENGEL
245 HAMMOND BLDG
UNIVERSITY PARK PA 16801

NO. OF
COPIES ORGANIZATION

2 PENN STATE UNIV
R MCNITT
C BAKIS
212 EARTH ENGR
SCIENCES BLDG
UNIVERSITY PARK PA 16802

1 PURDUE UNIV
SCHOOL OF AERO & ASTRO
C T SUN
W LAFAYETTE IN 47907-1282

1 STANFORD UNIV
DEPT OF AERONAUTICS
& AEROBALLISTICS
S TSAI
DURANT BLDG
STANFORD CA 94305

1 UNIV OF MAINE
ADV STR & COMP LAB
R LOPEZ ANIDO
5793 AEWB BLDG
ORONO ME 04469-5793

1 JOHNS HOPKINS UNIV
APPLIED PHYSICS LAB
P WIENHOLD
11100 JOHNS HOPKINS RD
LAUREL MD 20723-6099

1 UNIV OF DAYTON
J M WHITNEY
COLLEGE PARK AVE
DAYTON OH 45469-0240

1 NORTH CAROLINA ST UNIV
CIVIL ENGINEERING DEPT
W RASDORF
PO BOX 7908
RALEIGH NC 27696-7908

5 UNIV OF DELAWARE
CTR FOR COMPOSITE MTRLS
J GILLESPIE
M SANTARE
S YARLAGADDA
S ADVANI
D HEIDER
201 SPENCER LAB
NEWARK DE 19716

NO. OF
COPIES ORGANIZATION

1 DEPT OF MTRL
SCIENCE & ENGRG
UNIV OF ILLINOIS
AT URBANA CHAMPAIGN
JECONOMY
1304 WEST GREEN ST 115B
URBANA IL 61801

1 UNIV OF MARYLAND
DEPT OF AEROSPACE ENGRG
A J VIZZINI
COLLEGE PARK MD 20742

1 DREXEL UNIV
A S D WANG
3141 CHESTNUT ST
PHILADELPHIA PA 19104

3 UNIV OF TEXAS AT AUSTIN
CTR FOR ELECTROMECHANICS
J PRICE
A WALLS
J KITZMILLER
10100 BURNET RD
AUSTIN TX 78758-4497

3 VA POLYTECHNICAL
INST & STATE UNIV
DEPT OF ESM
M W HYER
K REIFSNIDER
R JONES
BLACKSBURG VA 24061-0219

1 SOUTHWEST RESEARCH INST
ENGR & MATL SCIENCES DIV
J RIEGEL
6220 CULEBRA RD
PO DRAWER 28510
SAN ANTONIO TX 78228-0510

1 BATELLE NATICK OPERS
B HALPIN
313 SPEEN ST
NATICK MA 01760

3 DIRECTOR
US ARMY RESEARCH LAB
AMSRD ARL WM MB
A FRYDMAN
2800 POWDER MILL RD
ADELPHI MD 20783-1197

NO. OF
COPIES ORGANIZATION

ABERDEEN PROVING GROUND

1 US ARMY ATC
CSTE DTC AT AC I
W C FRAZER
400 COLLERAN RD
APG MD 21005-5059

91 DIR USARL
AMSRD ARL CI
AMSRD ARL O AP EG
M ADAMSON
AMSRD ARL SL BA
AMSRD ARL SL BB
D BELY
AMSRD ARL WM
J SMITH
H WALLACE
AMSRD ARL WM B
A HORST
T KOGLER
AMSRD ARL WM BA
D LYON
AMSRD ARL WM BC
J NEWILL
P PLOSTINS
A ZIELINSKI
AMSRD ARL WM BD
P CONROY
B FORCH
M LEADORE
C LEVERITT
R LIEB
R PESCE RODRIGUEZ
B RICE
AMSRD ARL WM BF
S WILKERSON
AMSRD ARL WM M
B FINK
J MCCAULEY
AMSRD ARL WM MA
L GHIORSE
S MCKNIGHT
E WETZEL
AMSRD ARL WM MB
J BENDER
T BOGETTI
L BURTON
R CARTER
K CHO
W DE ROSSET
G DEWING
R DOWDING
W DRYSDALE

NO. OF
COPIES ORGANIZATION

R EMERSON
D HENRY
D HOPKINS
R KASTE
L KECSKES
M MINNICINO
B POWERS
D SNOHA
J SOUTH
M STAKER
J SWAB
J TZENG
AMSRD ARL WM MC
J BEATTY
R BOSSOLI
E CHIN
S CORNELISON
D GRANVILLE
B HART
J LASALVIA
J MONTGOMERY
F PIERCE
E RIGAS
W SPURGEON
AMSRD ARL WM MD
B CHEESEMAN
P DEHMER
R DOOLEY
G GAZONAS
S GHIORSE
C HOPPEL
M KLUSEWITZ
W ROY
J SANDS
D SPAGNUOLO
S WALSH
S WOLF
AMSRD ARL WM RP
J BORNSTEIN
C SHOEMAKER
AMSRD ARL WM T
B BURNS
AMSRD ARL WM TA
W BRUCHEY
M BURKINS
W GILLICH
B GOOCH
T HAVEL
E HORWATH
M NORMANDIA
J RUNYEON
M ZOLTOSKI

NO. OF
COPIES ORGANIZATION

AMSRD ARL WM TB
P BAKER
AMSRD ARL WM TC
R COATES
AMSRD ARL WM TD
D DANDEKAR
T HADUCH
T MOYNIHAN
M RAFTENBERG
S SCHOENFELD
T WEERASOORIYA
AMSRD ARL WM TE
A NIILER
J POWELL

NO. OF
COPIES ORGANIZATION

1	LTD R MARTIN MERL TAMWORTH RD HERTFORD SG13 7DG UK
1	SMC SCOTLAND P W LAY DERA ROSYTH ROSYTH ROYAL DOCKYARD DUNFERMLINE FIFE KY 11 2XR UK
1	CIVIL AVIATION ADMINSTRATION T GOTTESMAN PO BOX 8 BEN GURION INTRNL AIRPORT LOD 70150 ISRAEL
1	AEROSPATIALE S ANDRE A BTE CC RTE MD132 316 ROUTE DE BAYONNE TOULOUSE 31060 FRANCE
1	DRA FORT HALSTEAD P N JONES SEVEN OAKS KENT TN 147BP UK
1	SWISS FEDERAL ARMAMENTS WKS W LANZ ALLMENDSTRASSE 86 3602 THUN SWITZERLAND
1	DYNAMEC RESEARCH LAB AKE PERSSON BOX 201 SE 151 23 SODERTALJE SWEDEN

NO. OF
COPIES ORGANIZATION

1	ISRAEL INST OF TECHLGY S BODNER FACULTY OF MECHANICAL ENGR HAIFA 3200 ISRAEL
1	DSTO WEAPONS SYSTEMS DIVISION N BURMAN RLLWS SALISBURY SOUTH AUSTRALIA 5108 AUSTRALIA
1	DEF RES ESTABLISHMENT VALCARTIER A DUPUIS 2459 BLVD PIE XI NORTH VALCARTIER QUEBEC CANADA PO BOX 8800 COURCELETTE GOA IRO QUEBEC CANADA
1	ECOLE POLYTECH J MANSON DMX LTC CH 1015 LAUSANNE SWITZERLAND
1	TNO DEFENSE RESEARCH R IJSSELSTEIN ACCOUNT DIRECTOR R&D ARMEE PO BOX 6006 2600 JA DELFT THE NETHERLANDS
2	FOA NATL DEFENSE RESEARCH ESTAB DIR DEPT OF WEAPONS & PROTECTION B JANZON R HOLMLIN S 172 90 STOCKHOLM SWEDEN

NO. OF
COPIES ORGANIZATION

- | | |
|---|--|
| 2 | DEFENSE TECH & PROC
AGENCY GROUND
I CREWTHERR
GENERAL HERZOG HAUS
3602 THUN
SWITZERLAND |
| 1 | MINISTRY OF DEFENCE
RAFAEL
ARMAMENT DEVELOPMENT
AUTH
M MAYSELESS
PO BOX 2250
HAIFA 31021
ISRAEL |
| 1 | TNO DEFENSE RESEARCH
I H PASMAN
POSTBUS 6006
2600 JA DELFT
THE NETHERLANDS |
| 1 | B HIRSCH
TACHKEMONY ST 6
NETAMUA 42611
ISRAEL |
| 1 | DEUTSCHE AEROSPACE AG
DYNAMICS SYSTEMS
M HELD
PO BOX 1340
D 86523 SCHROBENHAUSEN
GERMANY |

INTENTIONALLY LEFT BLANK.